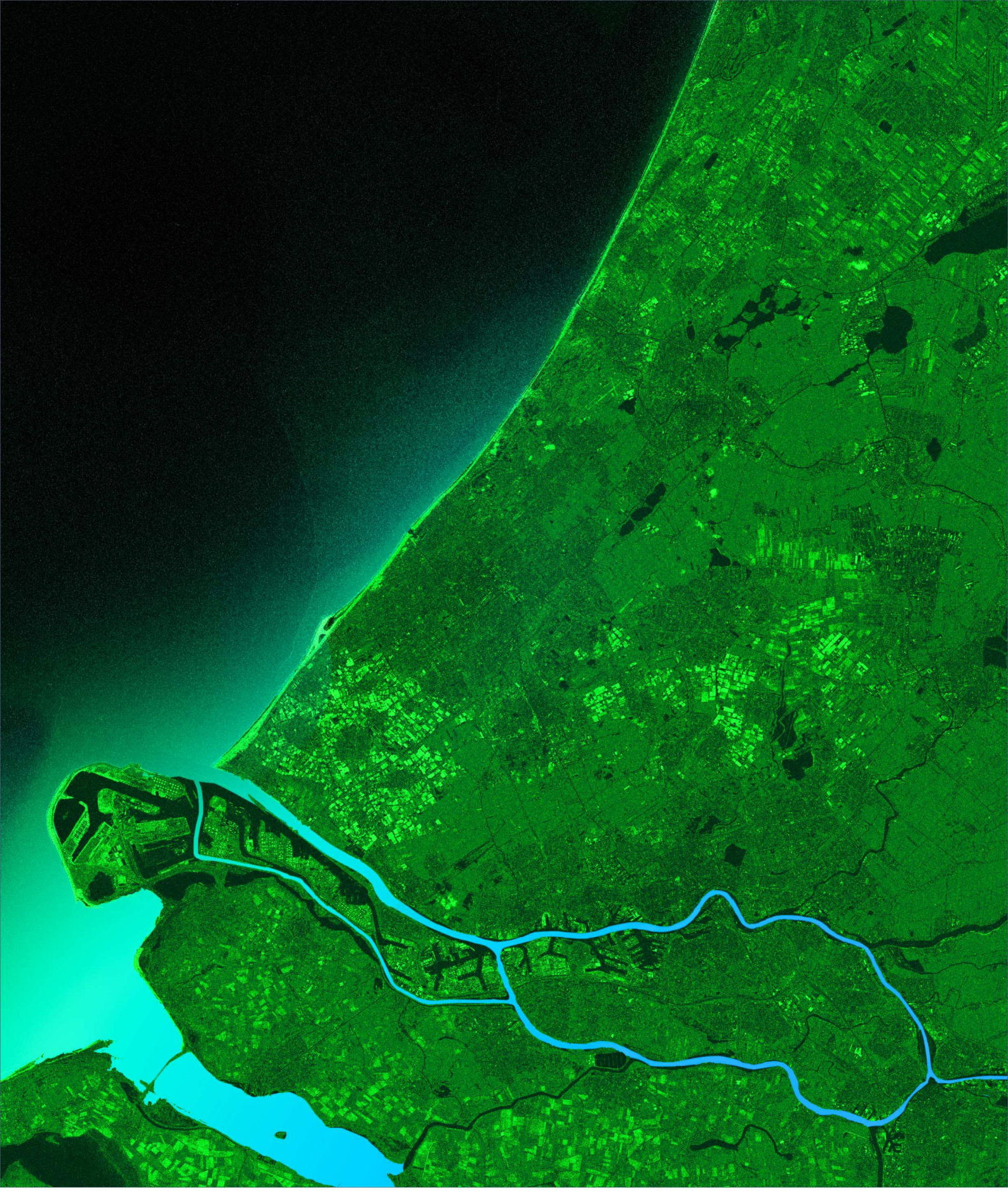

Nonlinear tides and river flow of estuarine networks

With a case study of the Rhine-Meuse

K.A. van der Riet

Nonlinear tides and river flow of estuarine networks
With a case study of the Rhine-Meuse

by

K.A. van der Riet

to obtain the degree of Master of Science
MSc. Climate Physics

First supervisor: Prof. dr. H.E. de Swart
Second supervisor: Prof. dr. L.R.M. Maas
Daily supervisor: J. Wang MSc.

Utrecht University

Student number: 4916189
October 2022

Abstract

Tides are important for the mixing and transport of sediments, salinity and nutrients in most estuaries around the world. Therefore, a precise understanding of the tides in estuaries is needed to predict changes over time. This research focuses on hydrodynamics and specifically on the mechanisms that result in nonlinear tides in networks of interconnected channels, which are known as estuarine networks.

To investigate this, a 2DV semi-analytical idealised model was developed that solves the hydrodynamics in estuarine networks. Here, two different networks were examined. First, the model was applied to an idealised three-channel network and subsequently the model was extended to the Rhine-Meuse estuarine network in the current state. Next, two scenarios are examined, studying the effect of respectively opening one of the Haringvliet sluices and 2-meters of sea-level rise on tides.

The results demonstrate that the model has been successfully applied to both networks. A comparison with observations for the Rhine-Meuse network showed good agreement for the linear tides (M_2). A fair agreement was found for the nonlinear tides (M_4). Here, the divergence of excess mass due to Stokes drift and no-stress condition have been proven as rhe most dominant mechanisms for the internal generation of nonlinear tides in this system. In addition, the externally forced M_4 tide was found to be a factor of 5-15 stronger than the internally generated M_4 tide.

Quantification of tidal asymmetry within the Rhine-Meuse has indicated that this system exhibits particularly flood dominant behaviour for both the water level and current velocity. Duration asymmetry showed strong flood dominance leading toward the middle part of the estuary, and then a decrease followed in the river part. Even stronger asymmetry was found for the velocity asymmetry throughout almost the whole system. Mixed behaviour was found for the flood-to-ebb ratio, with still predominantly flood dominant behaviour in most of the channels. It was also discovered that velocity asymmetry increases with the depth of the channels and the flood-to-ebb ratio decreases with depth. This emphasizes the importance of a 2DV model.

Concerning the two scenarios, the opening of one of the Haringvliet sluices demonstrated generally a slight increase in M_2 and M_4 elevation amplitudes and a combination of a slight increase/decrease for the current amplitudes, depending on the position in the network. The sea-level rise scenario revealed overall less impact on the tides than opening one of the Haringvliet sluices. Especially in the Haringvliet, an increase in M_2 elevation amplitude was found for this scenario. The M_4 elevation amplitude increased particularly in the Nieuwe Maas. The M_2 current amplitude showed an overall minor increase in the network, whereas for the M_4 current amplitude a combination of both minor increases/decreases was found.

Contents

1 Introduction

1.1 Hydrodynamics of estuarine networks

An estuary is a partially enclosed coastal body of water where freshwater from the rivers and saltwater from the ocean mix (Cameron and Pritchard, 1963; Valle-Levinson, 2010). Estuaries are one of the planet's most productive ecosystems because they are home to numerous plant and animal species. Many animals rely on them for food, and rest stops during migration and breeding grounds. In addition to ecological value, estuaries also represent great economic value. Tourism, fishing and leisure activities all profit economically from the commercial value and resources of these entities. Estuaries, which provide harbours and ports essential for shipping and transportation, also support significant public infrastructure in their protected coastal waters. Changes in the hydrodynamical and morphological conditions have an impact on how well these functions are fulfilled. Such changes are related to both human interventions and inherent variability. In many estuaries, tides play an important role in the mixing and transport of sediments, salinity and nutrients. Tides that propagate through an estuary affect the geometry by eroding and depositing sediments. In addition, human interventions to reduce flooding and ensure safe naval navigation are influencing the shape and structure of estuaries, and the latter, in turn, influences the tides.

Most studies focused on the dynamics of single-channel estuaries, e.g., Friedrichs (2010); Geyer and MacCready (2014). However, many estuaries consist of multiple interconnected channels. Examples of this are the Rhine-Meuse Estuary in the Netherlands, the Yangtze Estuary in China and the Ganges river Estuary in Bangladesh. An example of a single-channel estuary and estuarine network are shown in Figure 1.1. These network systems have numerous connections to the ocean, and freshwater can be transported via several routes from the river to the ocean.

Figure 1.1: Example of a single-channel estuary (Charente estuary in France) and estuarine network (Yangtze estuarine network in China). Source: Google Earth.

Locations in the estuarine network where different channels branch are described as vertex points. These vertex points are of pivotal importance to the water motion and distribution of freshwater in the network. The focus of this thesis is on tides and river flow in estuarine networks.

Tidal motion originates from the open ocean, where it is generated due to the earth's rotation about its axis and the relative motions of the sun, moon, and earth through tidal forces. As ocean tidal waves enter shallow coastal waters, they become deformed under the effects of channel convergence, friction and reflection. The principle of conservation of mass leads to an amplification of the tidal wave height in converging channels. Friction dampens the amplification of the tidal wave height and is strongly dependent on bed composition, water depth and internal friction caused by the viscosity and turbidity of the water (Prandle, 1997). Lastly, when a wave encounters a coastline or tidal weir, reflection occurs. The reflective wave leads to amplification or dampening of the tidal wave height depending on the phase of both the incoming and reflective wave.

In the open ocean, the tidal motion can be explained by some sinusoidal components. Typically, the major component is the semi-diurnal moon tide (M_2), in which case the ocean tide can be adequately characterized by a single sine function. Higher order components, for example, the M_4, can be internally generated by nonlinear processes as tidal waves progress into shallow coastal waters. The joint action of M_2 and M_4 tidal waves results in tidal asymmetry, as shown by, for instance, Parker (1991); Song et al. (2011). Nonlinear processes, such as the divergence of excess mass due to Stokes drift, the advection of momentum and nonlinear friction are the drivers of tidal asymmetry (see Parker (1991), for an explanation of these nonlinear processes). The phase difference between M_2 and M_4 tidal waves can be used to indicate tidal asymmetry (Friedrichs and Aubrey, 1988). A distinction must be made here between tidal asymmetry and tidal skewness. For the wave height, a phase difference between 0° and 180° lead to flood dominance due to the rising tide being shorter than the falling tide, whereas a phase difference between 180° and 360° degrees results in a shorter falling tide and thus ebb dominance. This type of tidal asymmetry is referred to as duration asymmetry. In addition to duration asymmetry, a phase difference can also lead to tidal skewness. In the context of wave height, tidal skewness assumes a tidal wave whose high-water peak is higher than the low-water peak, or vice versa depending on the phase difference. A pure skewed wave is found for a phase difference of exactly 0° or 180°. Figure 1.2 indicates both maximum tidal skewness and tidal asymmetry for the wave height.

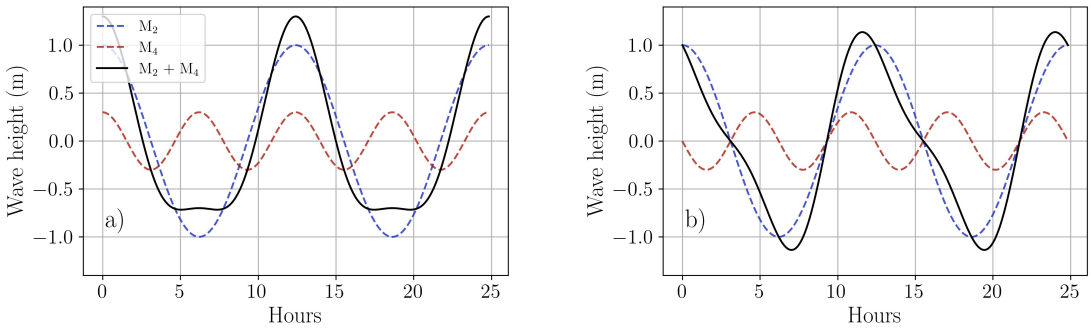

Figure 1.2: a) Time series of wave height for M_2, M_4 and combined wave with a phase difference of 0°, indicating maximal wave height skewness. b) As a), but a phase difference of 90°, indicating maximal duration asymmetry.

Similarly, tidal currents can become asymmetric, which is also called velocity asymmetry. A phase difference between the M_2 and M_4 currents in the range between 90° and 270° degrees denotes ebb dominance, while a phase difference between -90° and 90° degrees shows flood dominance (Friedrichs and Aubrey, 1988). In this case, a pure skewed current wave is found at exactly 90° or 270°. Skewness in this case leads to higher current velocities in either the flood or ebb phase of the wave.

Tidal asymmetry and skewness are particularly relevant in the context of sediment transport. One of the key factors in sediment transport and related large-scale morphological changes in tidal environments, such as estuaries, tidal inlets and coastal waters, is tidal asymmetry (Groen, 1967; Dronkers, 1986; Friedrichs and Aubrey, 1988). A difference in peak tidal currents between ebb and flood is a determining factor in net bedload transport of sediments, as shown by Aubrey (1986). Velocity asymmetry on the other hand also drives suspended load transport (Groen, 1967). This leads to the implication that both velocity asymmetry and skewness determine the direction and magnitude of net sediment transport.

While on one side of an estuarine network the tides and thereby salt water enters the system, on the other side the river, and thereby the freshwater enters. Changes in river discharge within a tidal cycle are typically small and for this reason, the river discharge is assumed as constant. The presence of both tidal and river flow within a network leads to changes in the dynamics due to the interaction between the two (Godin, 1999). This river-tide interaction results in internal and bottom friction parameters that not only depend on the horizontal and vertical structure of the network, but also on tides and river flow.

A quantitative understanding of the dominant nonlinear processes in an estuarine network is necessary to predict its changing behaviour over time and to assure that future human interventions can take place with higher precision. This thesis focuses on the hydrodynamics of estuarine networks and as a particular prototype system, the Rhine-Meuse Estuary in the Netherlands (Figure 1.3) will be studied. The general aim of this thesis is to gain a better understanding of the nonlinear processes within this particular estuary and to quantify how the changes affect tidal asymmetry.

Figure 1.3: Satellite image of the Rhine-Meuse estuarine network. The white lines are the channels considered in this study. The tidal wave enters the Rhine-Meuse at position 1. (Nieuwe Waterweg) and 2. (Hartelkanaal). At position 3. (Haringvliet) a dam and several sluices are located that close during flood and open during ebb. Source: Google Earth.

1.2 Current state of the research

Tidal wave propagation in a network of channels has long been studied and was first mentioned by Lorentz (1926), who developed a one-dimensional analytical model to predict tides and study their changes for the future construction of a dyke. Dronkers et al. (1959); Defant (1961) showed that solving the tidal motion at vertex points requires continuity of water level and conservation of mass. Hill and Souza (2006) have continued this research by developing a generic framework to analytically study any arbitrary estuarine network. However, only linear tides were considered in this study.

The knowledge of the distribution of river discharge at the vertex points was improved by Buschman et al. (2010); Sassi et al. (2011). Buschman et al. (2010) observed that the distribution of river discharge at the vertex point is influenced by tides for an idealised network and Sassi et al. (2011) further quantified the tidal impact on the subtidal discharge distribution at the vertex points by applying the theory to a real estuarine network. Alebregtse and de Swart (2016) further revised the theory of tidal wave propagation in an estuarine network by incorporating also the overtides. However, because this method is one-dimensional, it cannot resolve the vertical structure of the velocity in the network. Ianniello (1977) was the first to solve the vertical structure for single channel estuaries of constant width and depth and later for variable width and depth (Ianniello, 1979). Wang et al. (2021) extended the work of Ianniello (1977, 1979) by developing a model that resolves the vertical structure of the velocity in an estuarine network, though only linear tides were considered in this study.

On the Rhine-Meuse specifically, not many studies have been performed yet that investigate the hydrodynamics here. Van Wijngaarden (1999) developed a 2D model to study sediment transport in the Southern branch of the Rhine-Meuse. A more recent study was performed by Cox et al. (2021), in which they investigated the anthropogenic effects on sediment budget for different scenarios. Also, salt intrusion in the Rhine-Meuse has been an ongoing field of study within the SALTI-solutions research project (Pietrzak, JD, 2019) since 2019. One of the discussion points in recent years concerned the opening of the sluices of the Haringvliet during flood to stimulate the migration of fish in the Rhine-Meuse.

1.3 Objectives and research questions

As can be seen from the summary of the literature on estuarine networks, relatively little fundamental research has been done on overtides in a network. Only Alebregtse and de Swart (2016) consider overtides, however, this involves a one-dimensional approach with no focus on tidal asymmetry. In addition, no analytical studies have yet been conducted on the behaviour of tides and river flow and their role in tidal asymmetry within the Rhine-Meuse estuarine network. Analytical models are useful to identify processes or interactions in the simplest possible explanation (Murray, 2003). In summary, what is particularly missing from the current literature is studies that resolve overtides in estuarine networks and the subsequent consequence this has for tidal asymmetry. Motivated by the considerations given above, the following research questions are formulated:

$\mathcal{RQ}$ 1 What are the dominant nonlinear sources for tidal asymmetry in an estuarine network in each of the channels?

$\mathcal{RQ}$ 2 How does the magnitude of the externally forced M_4 tide compares to the magnitude of the internally generated M_4 tide in an estuarine network?

$\mathcal{RQ}$ 3 What type of asymmetry phenomena (flood or ebb dominant behaviour) occur in an estuarine network?

$\mathcal{RQ}$ 4 What will be the changes to the tides in the case of

1. the opening of one of the Haringvliet sluices?
2. sea level rise?

To improve the fundamental understanding of estuarine networks, an analytical model is first developed that solves tides and in particular overtides within a network and this was followed by applying this network model to the Rhine-Meuse estuarine network to find out which mechanisms are dominant in the generation of overtides and what this implies for tidal asymmetry. To address the research questions, the solution procedure for solving the hydrodynamics of single-channel estuaries from Ianniello (1977, 1979) will be used. Next, the method of Hill and Souza (2006) is followed to extend the solution of the hydrodynamics to an estuarine network. The network is then tested on an idealised three-channel system before being applied to the current conditions of the Rhine-Meuse. The asymmetry quantification measures introduced by Alebregtse and De Swart (2014) will be used to evaluate the degree of asymmetry within these systems. These quantification measures regard tidal range, flood-to-ebb ratio, duration of the falling tide and duration from flood to ebb. To address research question 4, two scenarios are examined with the Rhine-Meuse network model. First, the effects of opening one of the Haringvliet sluices on the tides within the Rhine-Meuse will be investigated. Second, the influence of sea level rise on the tides within the network will be examined. Both experiments are relevant since first of the intention is to open the Haringvliet sluices during flood more often. In addition, sea level rise is a current topic of discussion, especially for low-lying areas such as the Netherlands. An increase in sea level affects the tides within a system (Pickering et al., 2012) and this in turn changes the morphological conditions.

1.4 Thesis outline

Chapter 2 explains the model and its mathematical basis and methods. It also further details the different networks and experiments covered in this thesis. Chapter 3 includes the results of the network model for the different study sites for both tides and river flow as well as its implication on tidal asymmetry. Lastly, Chapter 4 and 5 contain the discussion and conclusions.

2 | Model and Methods

2.1 Model formulation

Before going into the equations of motion, it is important to first establish a definition for the different types of channels within an estuarine network. The following three types of channels will be defined:

1. **Sea channel**: This channel is forced on one side by a prescribed tidal elevation and the other side bounded by a vertex point.
2. **Middle channel**: This channel is on both sides bounded by a vertex point.
3. **River channel**: This channel is on one side constrained by a landward boundary and on the other side bounded by a vertex point.

An example network consisting of two 'river channels', one 'middle channel' and two 'sea channels is shown in Figure 2.1.

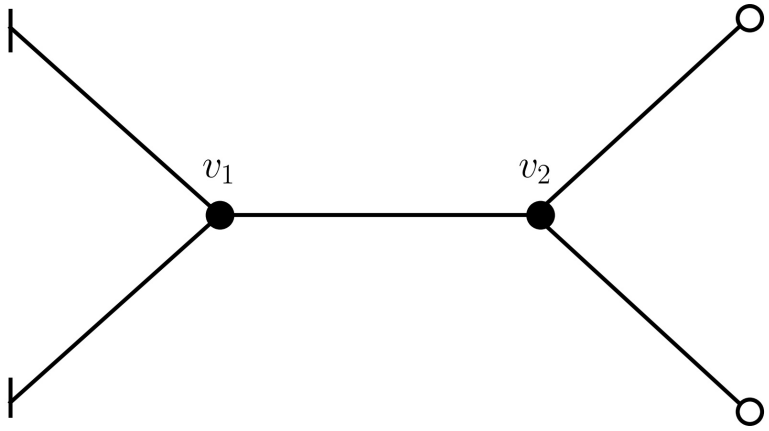

Figure 2.1: Example of a simple network consisting of two 'river channels', one 'middle channel' and two 'sea channels'. The vertical line denotes a landward boundary, the filled black dot displays a vertex point and the open black dot represents a seaward boundary.

To study the water motion in each of the channels, a width-averaged two-dimensional semi-analytical model will be developed that is based on earlier work for single-channel systems by Ianniello (1979). The positive x-axis is defined in the seaward direction and the z-axis points vertically upward. The width profile of every channel with length L_j, where j denotes the channel index, is assumed to be exponentially converging and is expressed as

$$B_j(x) = B_{L,j} \ \exp\left(\frac{x - L_j}{l_{b,j}}\right), \tag{2.1}$$

where $B_{L,j}$ is the width of the estuary at the seaward side of the channel and $l_{b,j}$ is the length over which the width of the channel changes by a factor exp . The channel index j is omitted from now on if the equations are the same for all channels. A sketch of the width profile as a function of the horizontal coordinate x is shown in Figure 2.2.

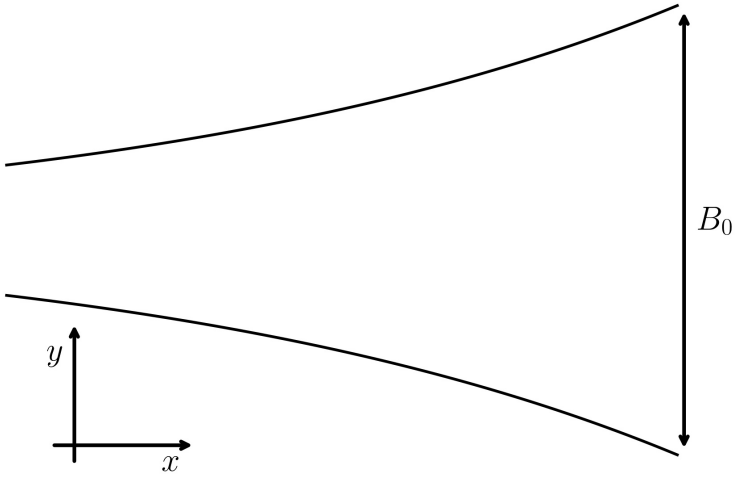

Figure 2.2: Sketch of width geometry. With x being the coordinate along the longitudinal direction and y being the coordinate along the transverse direction.

In this study, the effects of baroclinicity and the influence of tidal flats on the water motion are assumed to be negligible. Also, the local water depth is assumed to be constant in each channel and the turbulent transfer of energy is characterized by a spatial and temporal constant eddy viscosity A_v. The equations that describe the water motion are the momentum and continuity equations. These are the following

$$\frac{\partial u}{\partial t} + u\frac{\partial u}{\partial x} + w\frac{\partial u}{\partial z} = -g\frac{\partial \eta}{\partial x} + A_v\frac{\partial^2 u}{\partial z^2}, \tag{2.2}$$

$$\frac{\partial u}{\partial x} + \frac{\partial w}{\partial z} + \frac{1}{l_b}u = 0, \tag{2.3}$$

where u is the horizontal velocity, w is the vertical velocity, η is the sea surface elevation, g is the gravitational acceleration and H is the local water depth. On the left hand side of the momentum equation, the acceleration of the fluid is given by inertia in the first term

and advection terms are described in the second and third terms. The right hand side of the equation include respectively the barotropic pressure term and vertical turbulence term. The boundary conditions in the vertical direction for each channel are represented by

$$A_v \frac{\partial u}{\partial z} = 0 \text{ and } w = \frac{\partial \eta}{\partial t} + u\frac{\partial \eta}{\partial x}, \text{ at } z = \eta, \tag{2.4}$$

$$A_v \frac{\partial u}{\partial z} = \frac{\tau_b}{\rho} \text{ and } w = 0, \text{ at } z = -H. \tag{2.5}$$

Here ρ is the density of the fluid and τ_b is the bottom stress, which can be calculated by the quadratic friction law

$$\tau_b = \rho C_d^2 |u_b| u_b. \tag{2.6}$$

In this expression, C_d is the drag coefficient that is related to the roughness of the bed and u_b is the horizontal velocity at $z = -H$. Although the quadratic friction law applies to most tidal systems, difficulties in solving the equations arise when using this notation. The nonlinear bed stress can be circumvented by linearising the relation and relating the bottom stress to the eddy viscosity A_v. This linearisation can be written as

$$\tau_b = A_v \frac{\partial u_b}{\partial z} \approx \rho s_f u_b \tag{2.7}$$

where s_f is the partial slip-parameter, see, e.g., Csanady (1981). The assumption for this linearisation is that the total energy dissipation by the bottom friction is the same in the case of the quadratic stress as it is for the linearised stress. Here, the partial slip-parameter is assumed as constant in x. The eddy viscosity A_v is assumed as constant in x, z and t, but proportional to the depth of each channel as

$$A_v = \text{constant} \cdot H. \tag{2.8}$$

Here, the constant is taken as either a common value found in literature or tuned by observations. The depth-integrated continuity equation is used to solve for the surface elevation in each channel and it reads

$$\frac{\partial \eta}{\partial t} + \left(\frac{\partial}{\partial x} + \frac{1}{l_b}\right) \int_{-H}^{\eta} u \, dz = 0. \tag{2.9}$$

At the seaward end of the channels that are connected to the open sea, a M_2 and M_4 tidal wave are prescribed with amplitude Z_{M_2} and Z_{M_4} respectively. Their respective phases are given by φ_{M_2} and φ_{M_4}. At the river end of the channel, the river discharge Q is prescribed. This gives the following relations:

$$\eta = Z_{M_2} \cos(\omega t - \varphi_{M_2}) + Z_{M_4} \cos(2(\omega t - \varphi_{M_4})), \text{ at } x = L \text{ for sea channels,} \tag{2.10}$$

$$B \int_{-H}^{\eta} u \, dz = Q, \text{ at } x = 0 \text{ for river channels,} \tag{2.11}$$

where ω is the angular frequency of the M_2 tide. The remaining boundary conditions arise from the continuity of sea surface elevation and mass conservation on the vertex points. This can be expressed in the following way

$$\eta \text{ is continuous, at vertex points} \tag{2.12}$$

$$\sum B \int_H^\eta u \, dz \text{ is conserved, at vertex points} \tag{2.13}$$

For the conservation of mass equation, all the channels in which the fluid flow toward the vertex points are denoted with a plus-sign in front of the terms and all the channels in which the fluid leaves the vertex point are denoted with a minus sign in front.

2.2 Scaling and perturbation expansion

To evaluate the contribution of the individual terms, the dimensional system is transformed to a non-dimensional system by using the following dimensionless quantities:

$$x = L_{tide}\tilde{x}, \qquad \eta = Z_{M_2}\tilde{\eta}, \qquad t = \omega^{-1}\tilde{t}, \qquad z = H_0\tilde{z},$$

$$H = H_0\tilde{H}, \qquad u = U_0, \qquad w = W_0\tilde{w}, \qquad B = B_0\tilde{B},$$

where the variables with a tilde are the dimensionless variables, L_{tide} is the horizontal length scale, defined as $L_{tide} = \sqrt{gH_0}\omega^{-1}$, H_0 is the largest channel depth, B_0 is the largest width of the channel and U_0 and W_0 are the scales for respectively the horizontal and vertical velocity. The value for U_0 follows from the assumed approximate balance between inertia ($\frac{\partial u}{\partial t}$) and pressure gradient ($g\frac{\partial \eta}{\partial x}$) and substituting the definition for L_{tide} gives $U_0 = \frac{\omega Z_{M_2} L_{tide}}{H_0}$. The scaling for w follows from the approximate balance between the first two terms in the width-averaged continuity equation ($\frac{\partial u}{\partial x}$ and $\frac{\partial w}{\partial z}$), which are of the same order, and give $W_0 = \frac{H}{L_{tide}}U_0$. Inserting these relations in the momentum and continuity equations and then simplifying yields the final results of the scaling in the following non-dimensional system

$$\frac{\partial \tilde{u}}{\partial \tilde{t}} + \varepsilon\left(\tilde{u}\frac{\partial \tilde{u}}{\partial \tilde{x}} + \tilde{w}\frac{\partial \tilde{w}}{\partial \tilde{z}}\right) = -\frac{\partial \tilde{\eta}}{\partial \tilde{x}} + \hat{A}_v\frac{\partial^2 \tilde{u}}{\partial \tilde{z}^2}, \tag{2.14}$$

$$\frac{\partial \tilde{u}}{\partial \tilde{x}} + \frac{\partial \tilde{w}}{\partial \tilde{z}} + \frac{L_{tide}}{l_b}\tilde{u} = 0, \tag{2.15}$$

$$\frac{\partial \tilde{\eta}_n}{\partial \tilde{t}} + \left(\frac{d}{d\tilde{x}} + \frac{L_{tide}}{l_b}\right)\int_{-\tilde{H}}^{\varepsilon\tilde{\eta}_n} \tilde{u}_n \, d\tilde{z} = 0. \tag{2.16}$$

With the non-dimensional boundary conditions in the vertical plane

$$\hat{A}_v\frac{\partial \tilde{u}}{\partial \tilde{z}} = 0 \text{ and } \tilde{w} = \frac{\partial \tilde{\eta}}{\partial \tilde{t}} + \epsilon\tilde{u}\frac{\partial \tilde{\eta}}{\partial \tilde{x}}, \text{ at } \tilde{z} = \varepsilon\tilde{\eta}, \tag{2.17}$$

$$\hat{A}_v\frac{\partial \tilde{u}}{\partial \tilde{z}} = \hat{s}_f\tilde{u} \text{ and } \tilde{w} = 0, \text{ at } \tilde{z} = -\tilde{H}, \tag{2.18}$$

and in the horizontal plane

$$\tilde{\eta} = \cos(\tilde{t} - \varphi_{M_2}) + \tilde{Z}_{M_4}\cos(2(\tilde{t} - \varphi_{M_4})), \text{ at } \tilde{x} = \ell \text{ for sea channels,} \tag{2.19}$$

$$\tilde{B}\int_{-\tilde{H}}^{\tilde{\eta}} \tilde{u} \, d\tilde{z} = \tilde{Q}, \text{ at } \tilde{x} = 0 \text{ for river channels,} \tag{2.20}$$

$$\tilde{\eta} \text{ is continous, at vertex points,} \tag{2.21}$$

$$\sum \tilde{B} \int_{\tilde{H}}^{\varepsilon\tilde{\eta}} \tilde{u}\, dz \text{ is conserved, at vertex points.} \tag{2.22}$$

In equation 2.14 to 2.20, the following non-dimensional parameters appear

$$\varepsilon = \frac{Z_{M_2}}{H}, \tag{2.23}$$

$$\hat{A}_v = \frac{A_v}{H^2\omega}, \tag{2.24}$$

$$\tilde{Q} = \frac{Q}{U_0 B_0 H_0}, \tag{2.25}$$

$$\ell = \frac{L}{L_{tide}}, \tag{2.26}$$

$$\tilde{Z}_{M_4} = \frac{Z_{M_4}}{Z_{M_2}}, \tag{2.27}$$

$$\hat{s_f} = \frac{s_f}{H\omega}. \tag{2.28}$$

Here, ε is the Froude number that defines the relative importance of the different terms, $\hat{A}_v$ is the non-dimensional eddy viscosity, $\tilde{Q}$ is the non-dimensional river discharge, ℓ is the non-dimensional horizontal location at the seaward end of each channel, $\tilde{Z}_{M_4}$ is the non-dimensional M_4 elevation amplitude at ℓ of the sea channels and $\hat{s}_f$ is the non-dimensional slip-parameter. Next, it is important to describe the typical magnitudes for the derived non-dimensional variables. The parameter ε is much smaller than one, $\varepsilon = Z_{M_2}/H \ll 1$. The other parameters are compared to this ε. The variables with their assumed orders are provided in table 2.1.

Table 2.1: Non-dimensional variables with their order of magnitude.

Non-dimensional variable	**Order**
$\varepsilon \ll 1$	$\mathcal{O}(\varepsilon)$
$\tilde{A}_v$	$\mathcal{O}(1)$
$\frac{L_{tide}}{l_b}$	$\mathcal{O}(1)$
$\tilde{Q}$	$\mathcal{O}(\varepsilon)$
$\tilde{s}_f$	$\mathcal{O}(1)$
$\tilde{Z}_{M_4}$	$\mathcal{O}(\varepsilon)$

The non-dimensional discharge term $\hat{Q}$ is assumed here to be at order ε. This physically means that the river flow is much weaker than the tidal flow. Perturbation analysis allows the non-dimensional variables $\tilde{u}$, $\tilde{w}$ and $\tilde{\eta}$ to be described as power series of the variable ε as:

$$\tilde{u} = \tilde{u}_0 + \varepsilon\tilde{u}_1 + \mathcal{O}(\varepsilon^2), \tag{2.29a}$$

$$\tilde{w} = \tilde{w}_0 + \varepsilon\tilde{w}_1 + \mathcal{O}(\varepsilon^2), \tag{2.29b}$$

$$\tilde{\eta} = \tilde{\eta}_0 + \varepsilon\tilde{\eta}_1 + \mathcal{O}(\varepsilon^2). \tag{2.29c}$$

In these expressions, $\mathcal{O}$ denotes the respective order. Substitution of these variables in the equations of motion and boundary conditions and then subsequently collecting terms of equal order, leads to a representation of the system in which the dynamics can be studied at different orders.

2.3 Leading order system and solutions

For the leading order equations, the perturbation expansion is inserted in the non-dimensional momentum and continuity equations, then terms with $\mathcal{O}(1)$ are collected. The equations are made dimensional again with the use of the derived scaling arguments. From now on, the variables u, w and η will be denoted with two subscripts. The first subscript denotes the order of ε and the second subscript denotes the frequency of the examined tidal constituent. So, u_{02}, for example, represents the leading order horizontal velocity under examination of the M_2 tidal forcing. The dimensional equations of motion for the leading order read

$$\frac{\partial u_{02}}{\partial t} = -g\frac{\partial \eta_{02}}{\partial x} + A_v\frac{\partial^2 u_{02}}{\partial z^2}, \tag{2.30}$$

$$\frac{\partial u_{02}}{\partial x} + \frac{\partial w_{02}}{\partial z} + \frac{1}{l_b}u_{02} = 0, \tag{2.31}$$

$$\frac{\partial \eta_{02}}{\partial t} + \left(\frac{\partial}{\partial x} + \frac{1}{l_b}\right)\int_{-H}^{0} u_{02}\, dz = 0, \tag{2.32}$$

with the following dimensional boundary conditions

$$A_v\frac{\partial u}{\partial z} = 0 \text{ and } w = \frac{\partial \eta}{\partial t}, \text{ at } z = 0, \tag{2.33}$$

$$A_v\frac{\partial u}{\partial z} = s_f u \text{ and } w = 0, \text{ at } z = -H, \tag{2.34}$$

$$\eta = \cos(\omega t - \varphi_{M_2}), \text{ at } x = L \text{ for sea channels}, \tag{2.35}$$

$$B\int_{-H}^{\eta} u\, dz = 0 \text{ at at } x = 0 \text{ for river channels}, \tag{2.36}$$

$$\eta \text{ is continuous, at vertex points}, \tag{2.37}$$

$$\sum B\int_{H}^{0} u\, dz \text{ is conserved, at vertex points}. \tag{2.38}$$

The leading order equations allow the following solutions for u_{02}, w_{02} and η_{02}:

$$(u_{02}, w_{02}, \eta_{02}) = \Re\{(\hat{u}_{02}, \hat{w}_{02}, \hat{\eta}_{02})e^{-i\omega t}\}, \tag{2.39}$$

where $\Re.$ represents the real part of the variables and a hat denotes the complex amplitude of the variable that solely depends on the spatial structure. The solutions for $\hat{u}_{02}(x,z)$, $\hat{w}_{02}(x,z)$ and $\hat{\eta}_{02}(x)$ read after applying the vertical and horizontal boundary conditions

$$\hat{u}_{02}(x,z) = \frac{ig}{\omega}\frac{\mathrm{d}\hat{\eta}_{02}}{\mathrm{d}x}\left(\alpha_{M_2}\cosh(\gamma_{M_2}z) - 1\right), \tag{2.40}$$

$$\hat{w}_{02}(x,z) = -\frac{ig}{\omega}\left(\frac{\alpha_{M_2}}{\gamma_{M_2}}\sinh(\gamma_{M_2}z) - z\right)\left(\frac{\partial^2\hat{\eta}_{02}}{\partial x^2} + \frac{1}{l_b}\frac{\partial\hat{\eta}_{02}}{\partial x}\right) - i\omega\hat{\eta}_{02} \tag{2.41}$$

$$\hat{\eta}_{02}(x) = C_1 e^{k_1 x} + C_2 e^{k_2 x} \tag{2.42}$$

where $\gamma_{M_2} = \sqrt{-i\omega/A_v}$ and $\alpha_{M_2} = s_f(A_v\gamma_{M_2}\sinh(\gamma_{M_2}H) + s_f\cosh(\gamma_{M_2}H))^{-1}$. The complex wavenumbers k_1 and k_2 are given by:

$$k_{1,2} = \frac{-\frac{1}{l_b} \pm \sqrt{\left(\frac{1}{l_b}\right)^2 + \frac{4\omega^2}{g\left(\frac{\alpha_{M_2}}{\gamma_{M_2}}\sinh(\gamma H) - H\right)}}}{2}. \tag{2.43}$$

Here, C_1 describes the structure of the horizontal wave travelling in the positive x-direction and C_2 describes the structure of the wave in the negative x-direction. Values for the integration constants C_1 and C_2 can be found by applying boundary conditions of equations 2.10, 2.11 2.12. For sea channels, this means at the seaward end a tidal elevation is prescribed and a vertex points on the other side. Middle channels have vertex points on both sides and river channels have a vertex point on one side and on the other side, the current velocity goes to zero. When doing so, analytical expressions for the integration constants appear that depend on the elevation at the vertex point. The only unknowns in these equations is then η_{v_i}, with i the index of the vertex point. When these values are known, the whole system can be solved. To find these values, the analytical expressions for each type of channel are substituted in the mass conservation relation of equation 2.38. This system of linear equations can be solved numerically to obtain the values of the surface elevation at the vertex points. For a system with i-number of vertex points, this translates to the following matrix notation

$$\begin{bmatrix} D_{1,v_1} & D_{2,v_1} & \cdots & D_{n,v_1} \\ D_{1,v_2} & D_{2,v_2} & \cdots & D_{n,v_2} \\ \vdots & \vdots & \ddots & \vdots \\ D_{1,v_i} & D_{2,v_i} & \cdots & D_{n,v_i} \end{bmatrix} \cdot \begin{bmatrix} \eta_{v_1} \\ \eta_{v_2} \\ \vdots \\ \eta_{v_i} \end{bmatrix} = \begin{bmatrix} E_{v_1} \\ E_{v_2} \\ \vdots \\ E_{v_i}, \end{bmatrix}, \tag{2.44}$$

where the constants D_{n,v_i} and E_{v_i} are independent of the value of η at the vertex point and n is the index for the constants in the mass conservation relation. The constants E_{v_i} are solely determined by the characteristics of the sea channels in the case of linear tides.

Furthermore, the amplitudes for the elevation and current velocities can be found by taking the absolute value of the complex solutions. In addition, the phase is identified by computing the angle between the real and imaginary parts of the complex solutions. A full solution procedure for the leading order can be found in appendix A.1.

2.4 First order system

For the first order system of equations, all the terms with $\mathcal{O}(\epsilon)$ are collected. The dimensional first order system is given by

$$\frac{\partial u_1}{\partial t} + g\frac{\partial \eta_1}{\partial x} - A_v\frac{\partial^2 u_1}{\partial z^2} = \underbrace{-u_{02}\frac{\partial u_{02}}{\partial x} - w_{02}\frac{\partial u_{02}}{\partial z}}_{\text{advection}}, \tag{2.45}$$

$$\frac{\partial u_1}{\partial x} + \frac{\partial w_1}{\partial z} + \frac{1}{l_b} u_1 = 0, \tag{2.46}$$

$$\frac{\partial \eta_1}{\partial t} + \left(\frac{\partial}{\partial x} + \frac{1}{l_b} \right) \left(\int_{-H}^{0} u_1 \, dz + \underbrace{u_{02} \eta_{02}|_{z=0}}_{\text{Stokes}} \right) = 0, \tag{2.47}$$

The dimensional boundary conditions in the vertical are:

$$A_v \frac{\partial u_1}{\partial z} + \underbrace{A_v \eta_{02} \frac{\partial^2 u_{02}}{\partial z^2}|_{z=0}}_{\text{no-stress}} = 0 \text{ and } w_1 = \frac{\partial \eta_1}{\partial t}, \text{ at } z = \eta, \tag{2.48}$$

$$A_v \frac{\partial u_1}{\partial z} = s_f u_1 \text{ and } w_1 = 0, \text{ at } z = -H, \tag{2.49}$$

with the dimensional boundary conditions in the horizontal as:

$$\eta_1 = \underbrace{Z_{M_4} \cos\left(2(t - \varphi_{M_4})\right)}_{\text{external } M_4}, \text{ at } x = L \text{ for sea channels,} \tag{2.50}$$

$$\int_{-H}^{0} u_1 \, dz + u_{02} \eta_{02}|_{z=0} = \underbrace{\frac{Q}{B}}_{\text{river flow}} \quad \text{at } x = 0 \text{ for river channels,} \tag{2.51}$$

$$\eta \text{ is continuous, at vertex points,} \tag{2.52}$$

$$\sum B \int_{H}^{\eta} u \, dz \text{ is conserved, at vertex points.} \tag{2.53}$$

The underbraces denote the different nonlinear contributions in the equations that arise due to leading order interactions. This includes the contribution of *advection* of horizontal momentum, *no-stress* condition at the surface and the divergence of excess mass that compensates for the correlation between the horizontal velocity and sea surface elevation (*Stokes* drift), and the contribution due to *river flow*. Besides these internally created contributions to the first order flow, the system is forced by an externally prescribed overtide. Each of the different terms can be evaluated separately to study their relative importance. The first order contributions consist of a time-dependent and time-independent part. To illustrate this, the following solutions

$$u_{02} = \frac{1}{2} \hat{u}_{02} e^{-i\omega t} + \frac{1}{2} \hat{u}_{02}^* e^{i\omega t}, \tag{2.54a}$$

$$\eta_{02} = \frac{1}{2} \hat{\eta}_{02} e^{-i\omega t} + \frac{1}{2} \hat{\eta}_{02}^* e^{i\omega t}, \tag{2.54b}$$

where an asterisk denotes the complex conjugate, will be substituted in the horizontal advective contribution, this gives

$$\begin{aligned} -u_{02} \frac{\partial u_{02}}{\partial x} &= -\left(\frac{1}{2} \hat{u}_{02} e^{-i\omega t} + \frac{1}{2} \hat{u}_{02}^* e^{i\omega t} \right) \frac{\partial}{\partial x} \left(\frac{1}{2} \hat{u}_{02} e^{-i\omega t} + \frac{1}{2} \hat{u}_{02}^* e^{i\omega t} \right) \\ &= \underbrace{-\frac{1}{4} \left(\hat{u}_{02} \frac{\partial \hat{u}_{02}^*}{\partial x} + \hat{u}_{02}^* \frac{\partial \hat{u}_{02}}{\partial x} \right)}_{\text{time-independent}} \underbrace{-\frac{1}{4} \left(e^{-2i\omega t} \hat{u}_{02} \frac{\partial \hat{u}_{02}}{\partial x} + e^{2i\omega t} \hat{u}_{02}^* \frac{\partial \hat{u}_{02}^*}{\partial x} \right)}_{\text{time-dependent}} \end{aligned}$$

In this study, only the time-dependent part of advection, no-stress condition and the Stokes will be examined. The following notation can be made

$$(\eta_{14}, u_{14}) = (\eta_{14}, u_{14})_{\text{internal}} + (\eta_{14}, u_{14})_{\text{external}}, \tag{2.55a}$$

$$(\eta_{14}, u_{14})_{\text{internal}} = (\eta_{14}, u_{14})_{\text{Stokes}} + (\eta_{14}, u_{14})_{\text{no-stress}} + (\eta_{14}, u_{14})_{\text{advection}} \tag{2.55b}$$

In these expressions, the subscript 14 denotes the time-dependent part of each term. The contribution of river flow only has a time-independent part, since the change in river discharge during one tidal cycle is typically small.

2.4.1 First order solutions

M_4 solutions

In this section, a solution procedure will be provided for solving the first order (ε) system of equations in any of the channels in a network. The first order equations allow the following solutions for u_{14}, w_{14} and η_{14}:

$$(u_{14}, w_{14}, \eta_{14}) = \Re\{(\hat{u}_{14}, \hat{w}_{14}, \hat{\eta}_{14})e^{-2i\omega t}\}, \tag{2.56}$$

For the internally and externally generated overtide the following second-order non-homogeneous Ordinary Differential Equation (ODE) for the water level is found

$$\frac{\partial \hat{\eta}_{14}^2}{\partial x^2} + \frac{1}{l_b}\frac{\partial \hat{\eta}_{14}}{\partial x} - \frac{4\omega^2}{g\left(\frac{\alpha_{M_4}}{\gamma_{M_4}}\sinh(\gamma_{M_4}H) - H\right)}\hat{\eta}_{14} = F, \tag{2.57}$$

where $\gamma_{M_4} = \sqrt{-2i\omega/A_v}$ and $\alpha_{M_4} = s_f(A_v\gamma_{M_4}\sinh(\gamma_{M_4}H) + s_f\cosh(\gamma_{M_4}H))^{-1}$ and F is an additional forcing term. This differential equation is similar to the differential equation for the leading order elevation. The difference here is the addition of the forcing term F, which differs per contribution. For the externally prescribed M_4 tide, the equation is still homogeneous with F is 0. The higher frequency of the M_4 tide is incorporated in α_{M_4} and γ_{M_4}. A complete derivation for each of the forcing terms F per contribution as well as the solution for the horizontal velocity u_{14} can be found in Dijkstra et al. (2017a).

The solution for the sea surface elevation for each of the first order contributions has the following form

$$\hat{\eta}_{14}(x) = \underbrace{C_1 e^{p_1 x} + C_2 e^{p_2 x}}_{\text{homogeneous solution}} + \underbrace{A_1(x)e^{p_1 x} + A_2(x)e^{p_2 x}}_{\text{particular solution}}. \tag{2.58}$$

Obtaining values for the integration constants C_1 and C_2 is essentially the same procedure as for the leading order. The functions $A_1(x)$ and $A_2(x)$ of the particular solutions are already completely determined by the vertical structure of each channel. The constants in the homogeneous solution now must be chosen such that they satisfy the boundary conditions where $\eta_{14}(x)$ is determined by the sum of the homogeneous and particular solutions of the first order. If these relations are substituted in the mass conservation equation of equation 2.13, then the same matrix will appear for the first order network. The difference with the leading order is that the constants E_{v_i} are not solely determined by the sea channels, but now also depend on the characteristics of the middle and river channels in the network.

River flow

The river velocity in the network can be determined using the following derived equation

$$\hat{u}_{\text{river}} = g\left(\frac{z^2 - H^2}{2A_v} - \frac{H}{s_f}\right)\frac{\partial \hat{\eta}_{\text{river}}}{\partial x} \tag{2.59}$$

The expression for $\frac{\partial \hat{\eta}_{\text{river}}}{\partial x}$ follows from the substitution of the river velocity in the depth-integrated continuity equation and reads

$$\frac{\partial \hat{\eta}_{\text{river}}}{\partial x} = -\frac{Q}{gB(x)\left(\frac{H^3}{3A_v} + \frac{H^2}{s_f}\right)} \tag{2.60}$$

Now integrating equation 2.60 leads to an expression for the river surface elevation. A full solution procedure for the river flow can be found in Dijkstra et al. (2017a). In a network, Q for each channel is found by conservation of discharge at the vertex point.

2.5 Quantification of tidal asymmetry

In order to evaluate the degree of tidal asymmetry in the system, the spatial solutions for the leading and first order contributions need to be converted to time series as

$$\eta(x,t) = |\hat{\eta}_{02}|\cos\left(\omega t - \arg\left(\hat{\eta}_{02}\right)\right) + |\hat{\eta}_{14}|\cos\left(2\omega t - \arg\left(\hat{\eta}_{14}\right)\right) + \hat{\eta}_{\text{river}}, \tag{2.61a}$$

$$u(x,t) = |\hat{u}_{02}|\cos\left(\omega t - \arg\left(\hat{u}_{02}\right)\right) + |\hat{u}_{14}|\cos\left(2\omega t - \arg\left(\hat{u}_{14}\right)\right) + \hat{u}_{\text{river}}, \tag{2.61b}$$

where $\eta(x,t)$ and $u(x,t)$ are the full solutions in space and time with contributions from the leading order, first order and river flow. In these expressions, $|\cdot|$ denotes the amplitude of the solutions and $\arg(\cdot)$ denotes the phase. The river elevation and velocity only influence the skewness of the full solutions and do not affect the degree of tidal asymmetry and skewness within each channel. Following (Alebregtse and De Swart, 2014), four quantities are introduced to determine the degree of asymmetry of the system. These quantities are:

- **Tidal range**: Defined as the difference in sea surface elevation between flood and ebb during one tidal cycle for every position in the network.
- **Duration of the falling tide (DFT)**: Defined as the duration between peak flood elevation and peak ebb elevation on every position in the network. Relative to the tidal period, this quantity shows for values larger than 0.5 that flood crests move faster than ebb troughs, resulting in flood dominance. For values smaller than 0.5 this reveals that the ebb troughs propagate faster than the high water crests, resulting in ebb dominance. This quantity is also referred to as duration asymmetry.
- **Flood-to-ebb ratio**: Defined as the ratio between maximum flood current velocity and maximum ebb current velocity on every position in the network. Values higher than 1 reveal that flood currents move faster than ebb currents, and the flow is referred to as flood dominant. Values smaller than 1 reveal ebb dominant flows.

- **Duration between max flood and max ebb (DFE)**: Defined as the duration between peak flood current velocity and peak ebb current velocity on every position in the network. Relative to the tidal period, this quantity shows for values larger than 0.5 that a longer transition period is needed going from flood to ebb than the other way around. The opposite is the case for values smaller than 0.5. This quantity is also referred to as velocity asymmetry.

In figure 2.3, examples of the four quantities is given.

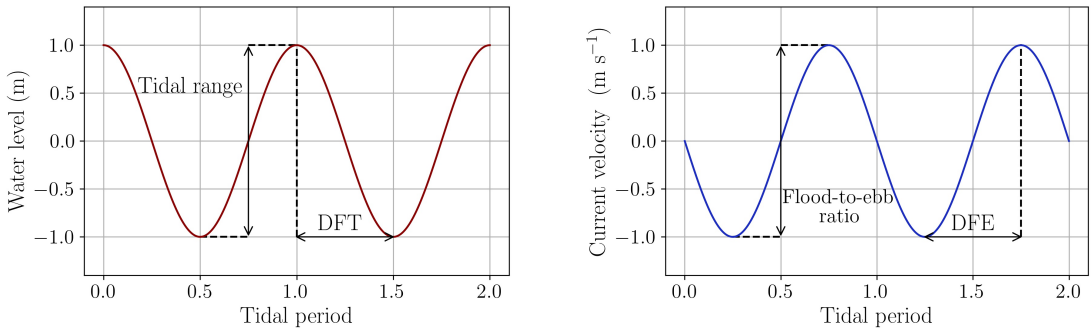

Figure 2.3: Time series of water level and current velocity to illustrate tidal asymmetry quantification (Tidal range, Flood-to-ebb ratio, Duration of the falling tide (DFT) and Duration from flood to ebb (DFE)), adopted from (Alebregtse and De Swart, 2014).

2.6 Settings of study sites

This subsection contains the regions of interest for this thesis. First a three channel system is modeled and analysed. This will be done to get acquainted with the model on a 'simple' network, before moving to a more complex estuarine network. Thereafter, the Rhine-Meuse estuarine network will be studied and results will be compared with in-situ data.

2.6.1 Three channel network

The three channel network that is considered in this first study is shown in Figure 2.4.

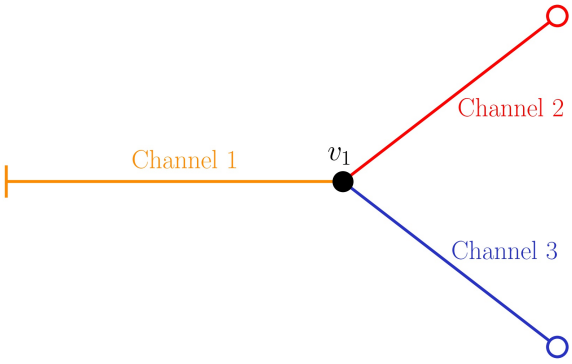

Figure 2.4: Sketch of the three channel network, consisting of one river channel and two sea channels. Colour coding and labels are consistent in further figures.

Here, channel 1 is the river channel, constrained by the landward boundary at $x = 0$ and channels 2 and 3 are both sea channels with a prescribed tidal forcing at $x = L$. The values for the variables H, B and L at each of the channels are found in table 2.2. The convergence length scale l_b is not shown, since all channels are considered to be straight. The eddy viscosity is taken as a constant in both the vertical and horizontal direction and proportional to the channel depth H, as $A_v = 0.0005\ H\ (\mathrm{m\,s^{-1}})$. The partial slip-parameter s_f is assumed to be constant throughout the network with a value of $0.001\ \mathrm{m\,s^{-1}}$. The values for all the parameters in this model are based on work by Wang et al. (2022). This network acts as a prototype system before studying a more complex network.

Table 2.2: Values for the variables H, B and L at each of the channels in the idealised network.

	H (m)	B_0 (m)	L (km)
Channel 1	13.0	1000	1040
Channel 2	15.0	500	40
Channel 3	11.0	500	40

2.6.2 Rhine-Meuse estuarine network

The Rhine-Meuse estuarine network will be used as the second network for this study. This estuary is located in the west of the Netherlands and is connected to the open sea through the Nieuwe Waterweg and Hartelkanaal. On the other end, freshwater enters the system through the Maas river and through some rivers connected to the Rhine, e.g., the Waal.

The hydrodynamics of the Rhine-Meuse estuarine network is considered on the domain shown schematically and in a satellite image in Figure 2.5. This network consist of two sea channels, three middle channels, one river channels and one special channel. Here, the Haringvliet (HV) used to be a sea channel but has been closed since the year 1971 with a dam and several sluices to protect the land around the Rhine-Meuse estuary. However, the sluices open during ebb to discharge water from the river to the sea. For this study, the channels that are expected to make a significant contribution to the hydrodynamics of the Rhine-Meuse are included. Some smaller channels and passages considered as not important to the overall hydrodynamics in this network are not evaluated. Also, the Waal river (WL) is the only connected river in this model, since this river conveys the largest part of the discharge.

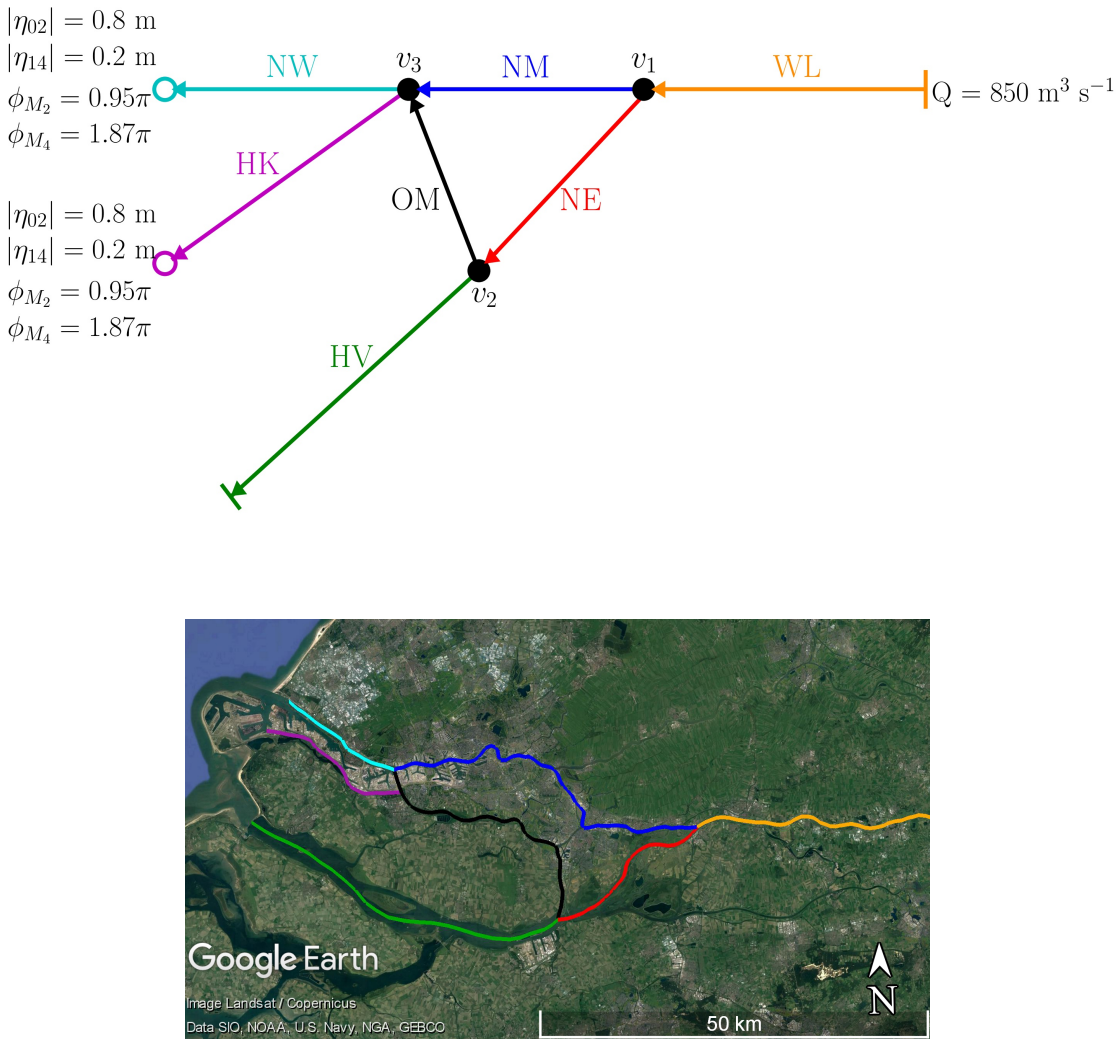

Figure 2.5: First panel: schematic diagram for the Rhine-Meuse estuarine network with prescribed tidal forcings and phases on the left of the sea channels. The arrows point in the direction of the positive x-axis in every channel. Second panel: Satellite image of the Rhine-Meuse (Source: Google Earth). The color coding will be consistent in further figures.

Note that the positive x is towards the left. The water motion in the network is forced by M_2 and M_4 tides at the seaward boundaries, with amplitudes of respectively 0.8 and 0.2 meters. At the river end of network, a river discharge of 850 $m^3\,s^{-1}$ is prescribed. This value is based on the average discharge of monitoring stations in September 2022 (Rijkswaterstaat, 2022a). The values for the variables H, B, L and l_b at each channel is found in table 2.3.

Table 2.3: Values for the variables H, B, L and l_b at each of the channels. Source: N. Vellinga, pers. comm. and Google Earth. Note that some channels are the combination of multiple channels.

	H (m)	B_0 (m)	L (km)	l_b (km)
Nieuwe Waterweg (NW)	15.0	700	16.4	-217.3
Hartelkanaal (HK)	7.6	331	21.7	-298.0
Nieuwe Maas / Noord / Beneden Merwede (NM)	8.0	450	47.5	56.0
Nieuwe Merwede (NE)	5.0	420	23.4	53.9
Oude Maas / Dordtsche Kil (OM)	10.0	320	35.8	160.4
Boven Merwede / Waal (WL)	5.0	450	95.0	296.5
Haringvliet / Hollands Diep (HV)	8.0	2200	44.5	-146.0

2.6.3 Optimization with measurement stations

Along the Rhine-Meuse, eleven Rijkswaterstaat monitoring stations have been positioned to track local water levels over time. Data from these monitoring stations over the past two months are used to determine the amplitude of the M_2 and M_4 tides at the seaward end on one hand and to optimize the friction parameters A_v and s_f on the other hand. This data is available through Rijkswaterstaat (2022b). A harmonic analysis using the Python library T_{tide} (Pawlowicz et al., 2002) is used here to translate the local water level to each of the frequency components. After obtaining the M_2 amplitudes at each of the monitoring stations, the network model is run for one hundred variations in A_v in a range between 0.0001 and $0.01{\cdot}H$ ($\mathrm{m\,s^{-1}}$) and one hundred variations in s_f in the range 0.001 and 0.1 $\mathrm{m\,s^{-1}}$, yielding a total number of ten thousand model runs. From each of the runs, the Root-Mean-Square-Error (RMSE) between model and observations is determined. The combination of A_v and s_f for which the RMSE is minimized is then adopted as friction parameters in the remainder of this report.

2.6.4 Experiments on the RM network

To address the fourth research question, two additional scenarios are conducted on the Rhine-Meuse network to find out how much influence these experiments have on the evolution of the tides.

Opening of the Haringvliet sluice during high tide

Since their construction in the early 1970s, the Haringvliet sluices have kept the southwestern Netherlands safe from flooding. However, the sluices act as a fish barrier between the North Sea and the Haringvliet. This prevents migratory fish like eels, salmon, and sea trout from swimming to their spawning grounds, which are either upstream or in the sea. By opening the Haringvliet sluices at high tide, migratory fish can swim downstream pf the Haringvliet with the salty water. For this experiment, one of the Haringvliet sluices will be opened, whose

influence on tidal propagation will be investigated. This means for the estuarine network that this channel is converted from a river channel to a sea channel. The width of the opening is taken as 57.5 meters (source: Rijkswaterstaat, pers. comm.), the length of the sluice is determined at 70 meter (source: Google Earth).

A one-dimensional approximation will be made to determine the corresponding M_2 amplitude at the seaward side of the Haringvliet. Given the fact that the opening of the sluice is small relative to the width of the Haringvliet, it is assumed that in the sluice friction dominates over inertia. This gives a balance between pressure gradient and friction as

$$-g\frac{\partial \eta}{\partial x} = \lambda u, \tag{2.62}$$

where λ is a one-dimensional friction parameter. Furthermore, continuity of sea surface elevation and conservation of mass apply here

$$\eta_1 = \eta_2, \tag{2.63}$$

$$u_1 B_1 = u_2 B_2, \tag{2.64}$$

where the subscripts 1 and 2 represent respectively the position at the beginning of the sluice and at the end of the sluice. The velocity at the beginning of the sluice can also be found by integrating the momentum balance, this gives

$$u_1 = (\eta_1 - \eta_2)\frac{g}{\lambda L_{\text{sluice}}} \tag{2.65}$$

where $\eta_1 = 0.8$ meters is the amplitude at the seaward side. To start, an arbitrary value for u_1 is chosen. A value for u_2 can found by using the mass conservation balance. The network model is then used to find a value for η_2. Lastly, equation 2.65 is used to find a new value for the velocity at the beginning of the sluice. The absolute value between the difference of the initial velocity and the new velocity is used as a error tolerance. This procedure repeats until the error tolerance in the velocity converges to a value smaller than 10^{-5} $\mathrm{m\,s^{-1}}$. The final velocity, using this method, is determined at 2.46 $\mathrm{m\,s^{-1}}$. This translates to a sea surface elevation of 0.095 meters. The external M_4 amplitude at the seaward end is taken with the same relative decrease as the M_2, this gives 0.024 meters. This value will now be used as the amplitude at the seaward side of the Haringvliet.

Consequence of sea-level rise (SLR)

Long-term average sea-level rise relative to local land level, as measured by coastal tide gauges, is referred to as sea-level rise. Global sea level rise is currently estimated to be between 3 and 4 millimetres per year, with an acceleration of 0.12 ± 0.07 mm $\mathrm{yr^{-2}}$ (Oppenheimer et al., 2019). In this experiment, the influence of 2-meter sea level rise on the tides in the Rhine-Meuse is investigated. A rise of 2 meters is assumed as an upper limit by the year 2100 (Pfeffer et al., 2008) and as a higher probability scenario for the year 2200 (Vellinga et al., 2009). The sea level rise scenario is modeled by deepening each channel of the Rhine-Meuse by 2 meters. Also, the amplitude of the M_2 and M_4 tide on the seaward side is increased by 6 and 1.5 cm, respectively, (Pickering et al., 2012).

3 Results

3.1 Results for the idealised network

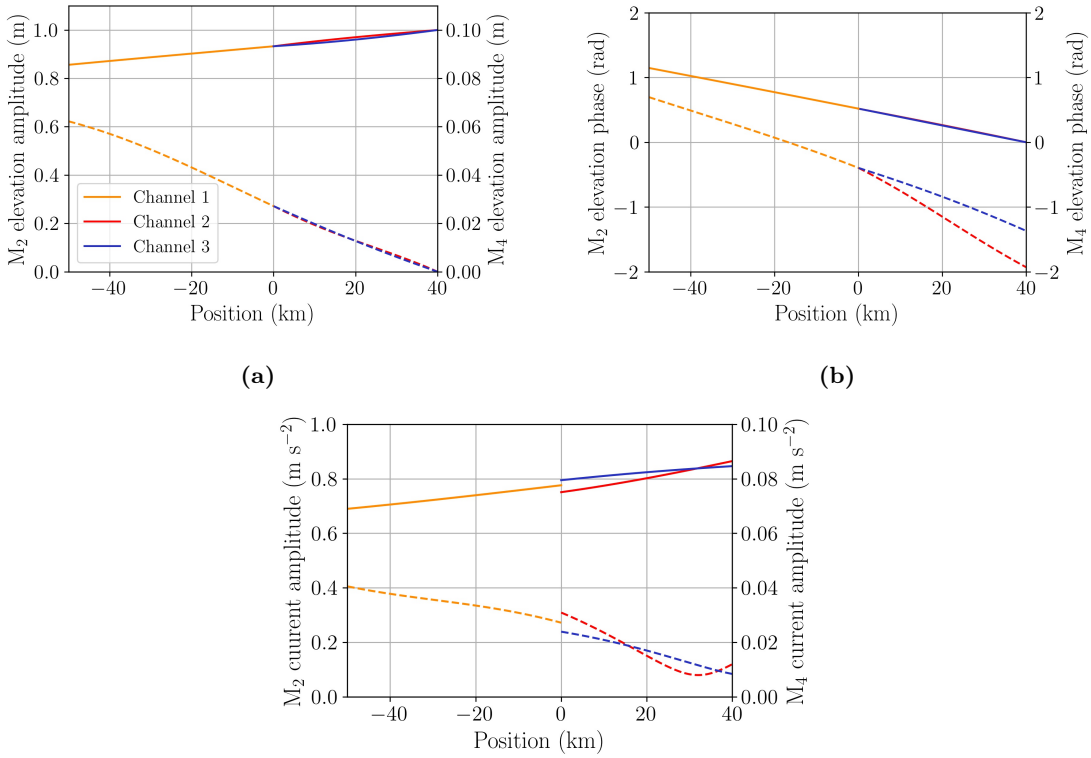

Figure 3.1: a) M_2 (solid lines) and M_4 (dashed lines) elevation amplitudes as a function of position in the network. b) As a), but for elevation phases. c) As a), but for current amplitudes.

The results for the idealised network are shown in Figure 3.1. In these panels, 50 km before the vertex point and 40 km after the vertex point in the horizontal direction are shown to capture the behaviour of the tides around this point.

Figure 3.1 shows a decrease in M_2 elevation amplitude in every channel towards the landward boundary. Part of the decrease in amplitude can be attributed to the dissipation of energy to the higher harmonics. This is evidenced by the increase in the internally generated M_4 amplitude, which increases towards the landward boundary. The elevation phases for M_2 and M_4 in Figure 3.1b illustrates propagating behaviour in the landward direction for every channel (negative $\mathrm{d}\phi/\mathrm{d}x$, where ϕ is the elevation phase) with increasing phase towards negative x. Figure 3.1c shows similar behaviour for M_2 and M_4 current amplitudes as was found for the M_2 and M_4 elevation, with decreasing amplitude for the M_2 component and increasing amplitude for the M_4 amplitude towards the landward boundary.

This exact set up is also used by Wang et al. (2022). The only difference is that this study also included the influence of dynamic pressure as a source of internally generated M_4. Comparison of the results, however, shows that the influence of that source is small compared to the other nonlinear contributions. The M_2 elevation and current amplitudes are almost identical in both studies. This thesis expands on the work by Wang et al. (2022) by connecting the results to tidal asymmetry. For this three-channel system the quantification of asymmetry is shown in Figure 3.2.

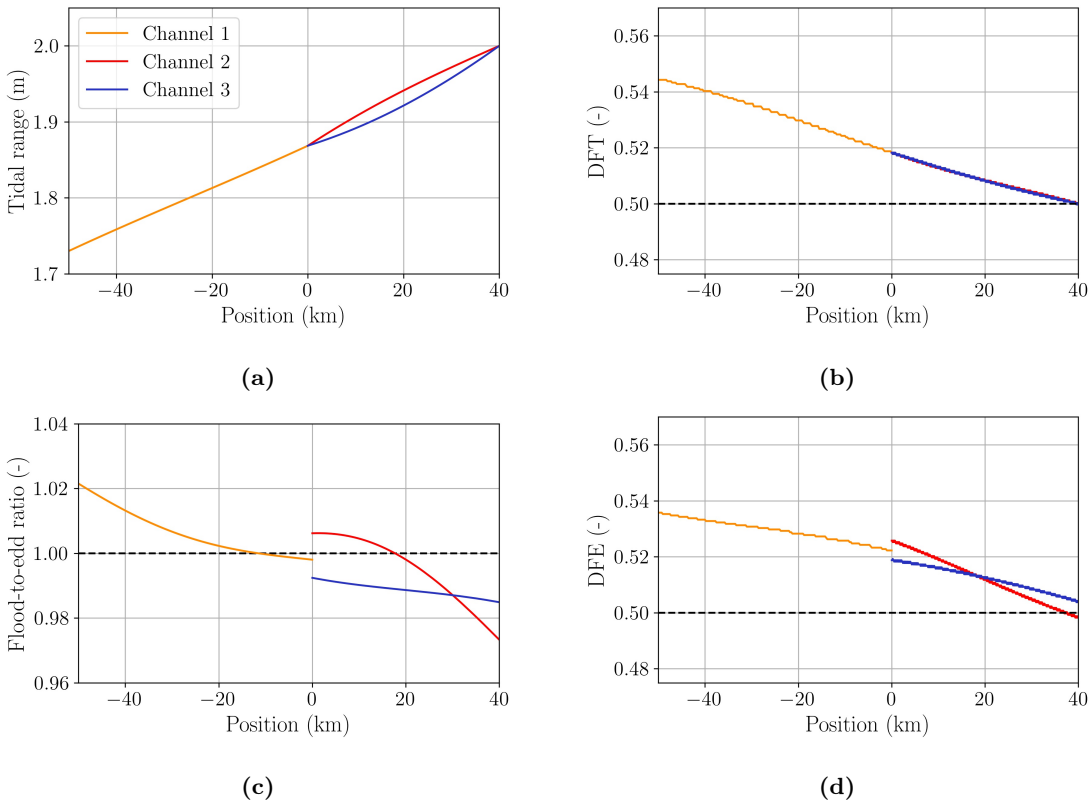

Figure 3.2: a) Tidal range as function of the position in the network. b) As a), but for DFT. c) As a), but for Flood-to-ebb ratio. d) As a, but for DFE.

Figure 3.2a shows the tidal range as a function of the position in the network. The pattern shows similarities with the M_2 elevation amplitude, with decreasing values towards the landward boundary. Figure 3.2b shows the DFT. This figure reveals flood dominant behaviour, with DFT greater than 0.5 everywhere in the network. This means that high water crests propagate faster than low water troughs. Mixed behaviour is found for the currents. The Flood-to-ebb ratio in Figure 3.2c shows ebb dominant behaviour in the entire channel 3 and the first half of channel 2. Flood dominant currents are found in the second half of channel 2 and the majority of channel 1. This means that, when only considering M_4 tides as source of asymmetry, bedload transport of sediment occurs in the ebb direction for channel 3 and the majority of channel 2. For channel 1, bedload transport would occur in the opposite direction. Finally, Figure 3.2d illustrates the DFE as a function of the position in the network. This figure shows flood dominance for every channel, with DFE greater than 0.5 throughout the network. This means that it takes more time for the system to transition from flood to ebb than the other way around. Velocity asymmetry is important for suspended sediment transport. This means that in this system transport of suspended sediments landward would occur. The remainder of the results in this chapter will address the extension of the network to the Rhine-Meuse.

3.2 Results for the Rhine-Meuse estuarine network

3.2.1 M_2 tide

The values of the eddy viscosity A_v and partial slip-parameter s_f are chosen such that the Root Mean Square Error (RMSE) between modelled and observed elevation amplitudes is minimized. This calibration resulted in values of $0.00144 \cdot H$ ($\mathrm{m\,s^{-1}}$) and 0.06555 $\mathrm{m\ s^{-1}}$ for respectively the eddy viscosity and the partial slip-parameter. The eddy viscosity scales with the depth of the channels, meaning that the eddy viscosity is the largest in the deepest channel (NW) and the smallest in the shallowest channel (WL). The results for the leading order in the Rhine-Meuse are presented in Figure 3.3.

The M_2 elevation amplitudes in Figure 3.3a show that there is a good agreement between the modelled elevation amplitudes and the observed elevation amplitudes, with a RMSE of 0.048 meters. The largest discrepancy between the model and observations in the network can be found at the second point of the Nieuwe Maas (NM). This difference can be attributed to the fact that in the modelled network both the sea channels and the NM and OM channels branch at the same vertex point, whereas in reality there exists a short passage that connects the vertex point between the NM and the NW with the vertex point of the HK and OM. The overall modelled tidal damping in the network agrees good with the observed tidal damping. The elevation phases in Figure 3.3b indicate a propagating wave in the direction of the landward boundary (negative phase speed) for both the sea channels, the NM and OM middle channels and the WL river channel. A propagating wave in the direction of the seaward boundary is shown for the HV channel (positive phase speed). Lastly, the NE shows a change from a negative phase speed at the seaward end to a positive phase speed at the landward end of the channel. This indicates the presence of a dominant reflective wave in this channel. Typical phase speed values in the network range from 3 $\mathrm{m\,s^{-1}}$ (large $\mathrm{d}\phi/\mathrm{d}x$) to 13 $\mathrm{m\,s^{-1}}$ (small $\mathrm{d}\phi/\mathrm{d}x$).

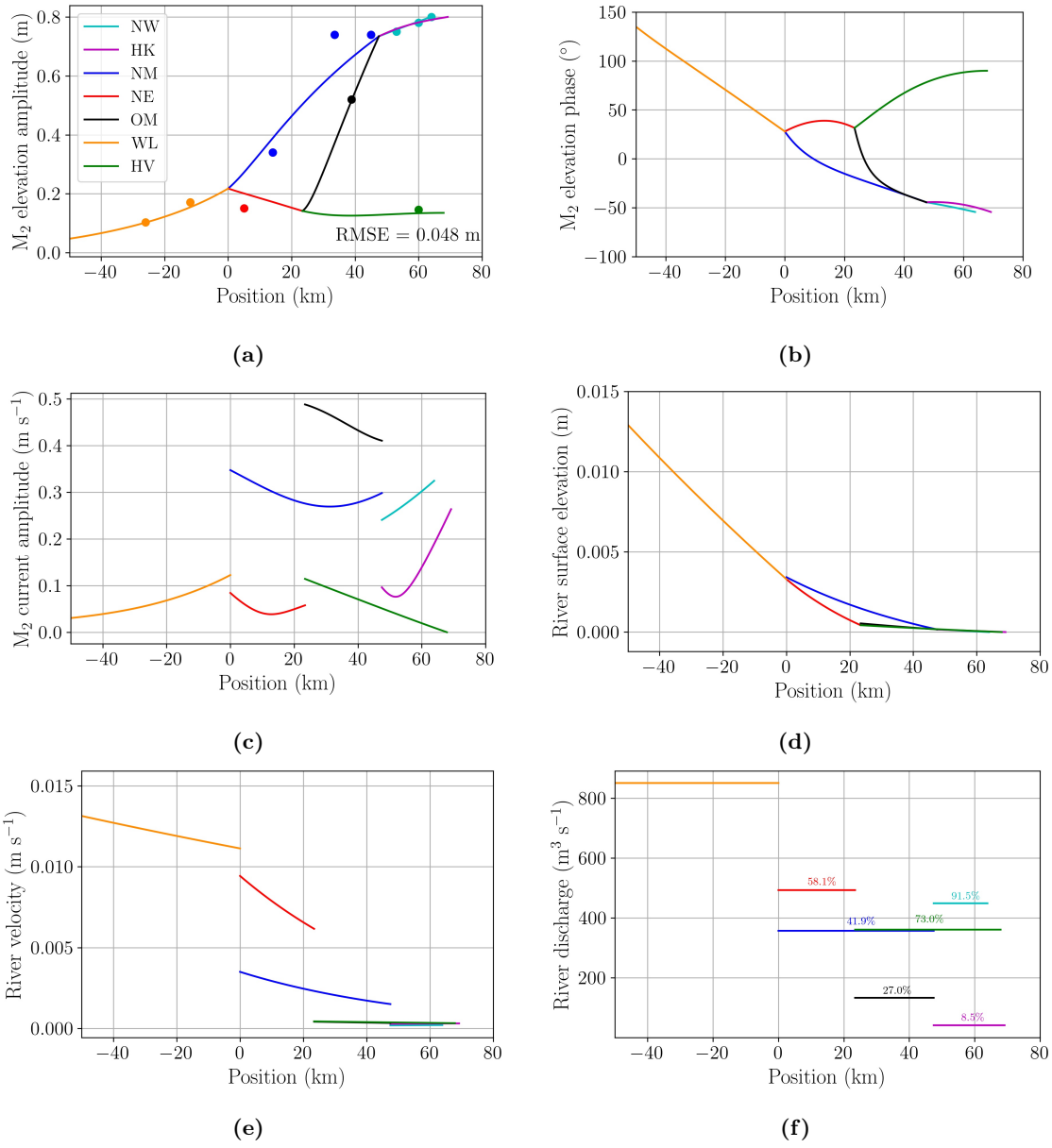

Figure 3.3: a) M_2 elevation amplitudes as a function of position in the Rhine-Meuse network The coloured dots in a) represent M_2 elevation amplitude observations. b) As a), but for elevation phases. c) As a), but for depth-averaged current amplitudes. d) As a), but for river surface elevation. e) As a), but for river velocity. f) As a) but for river discharge. The percentages are a measure for the relative discharge after a vertex point. Note: the figures are horizontally flipped with respect to the schematic figure shown in Figure 2.5 because the network model is built on a seaward side on the right side.

Figure 3.3c indicates differences in increase or decrease of M_2 current amplitude per channel. The complexity can be mainly attributed to the differences in convergence length per channel and its interplay with friction. The M_2 current amplitude in the Nieuwe Merwerde (NE) is much lower than was found for the other two middle channels. With almost no difference in velocity between both sides of the channel, just as for the elevation amplitude in this channel. This shows that this particular channel is not so important for the overall hydrodynamics in the system. Figure 3.3d shows the river elevation in the Rhine-Meuse. This figure reveals that the influence of the river on the total elevation small is compared to the influence of the M_2 tide in the majority of the network. However, an opposite pattern to the M_2 elevation is visible with increasing values towards the landward end. This means that the influence of the river, as expected, becomes more important as the tide progresses land inwards. The depth-averaged river velocity is shown in Figure 3.3e. This figure reveals a similar pattern as was shown for the river surface elevation, with increasing velocities towards the landward end of the network. Finally, Figure 3.3f demonstrates the distribution of freshwater in the network. The percentages are a measure of the relative discharge after a vertex point. The largest difference in distribution is found between the two sea channels, with a relative contribution of 91.5% and 8.5% for respectively the Nieuwe Waterweg (NW) and Hartelkanaal (HK). This can be explained by the difference in width and depth between the two channels. The Nieuwe Waterweg is approximately twice as wide and deep as the Hartelkanaal. The river discharge is strongly dependent on both of these factors. It is shown here that the opening of the Haringvliet during ebb is important for the discharge of river water, with also a significant amount of the total discharge.

The M_2 current amplitudes over both the vertical and horizontal direction for the Nieuwe Waterweg (a) and Nieuwe Maas (b) are presented in Figure 3.4.

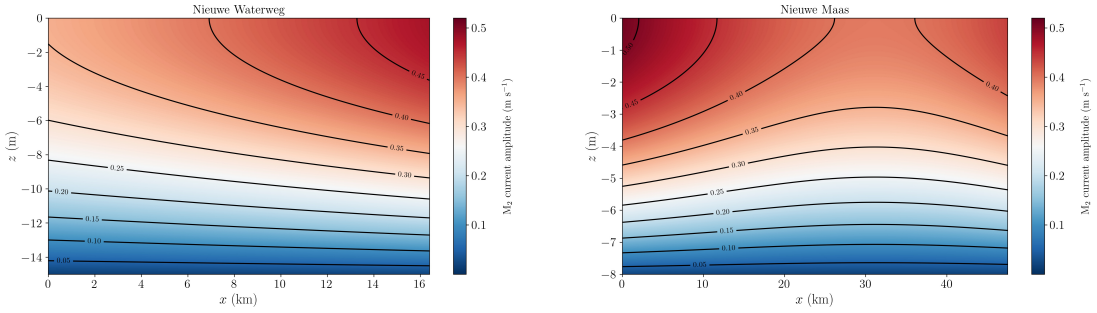

(a) **(b)**

Figure 3.4: Contour plots of M_2 current amplitudes profiles over x and z for Nieuwe Waterweg (a) and Nieuwe Maas (b).

Figure 3.4 indicates for both channels a clear gradient in the M_2 current amplitude over the vertical direction of the channel. The lowest currents are found near the bed of the channels (partial slip) and highest currents are located near the surface. These current amplitude figures stress the usefulness of a 2DV modelling approach. When considering the transport of sediments in estuaries it is important to understand the vertical structure of the current amplitude, as this is what drives the transport.

3.2.2 Internally created M_4 tide

This study differentiates between an internally and externally generated M_4 tide. The results for the internally generated M_4 tide in the Rhine-Meuse including the contribution of divergence of excess mass due to Stokes drift, no-stress condition and advection of horizontal momentum are shown in Figure 3.5 for the M_4 elevation amplitude, M_4 elevation phase, depth-averaged M_4 current amplitude and M_4 current phase.

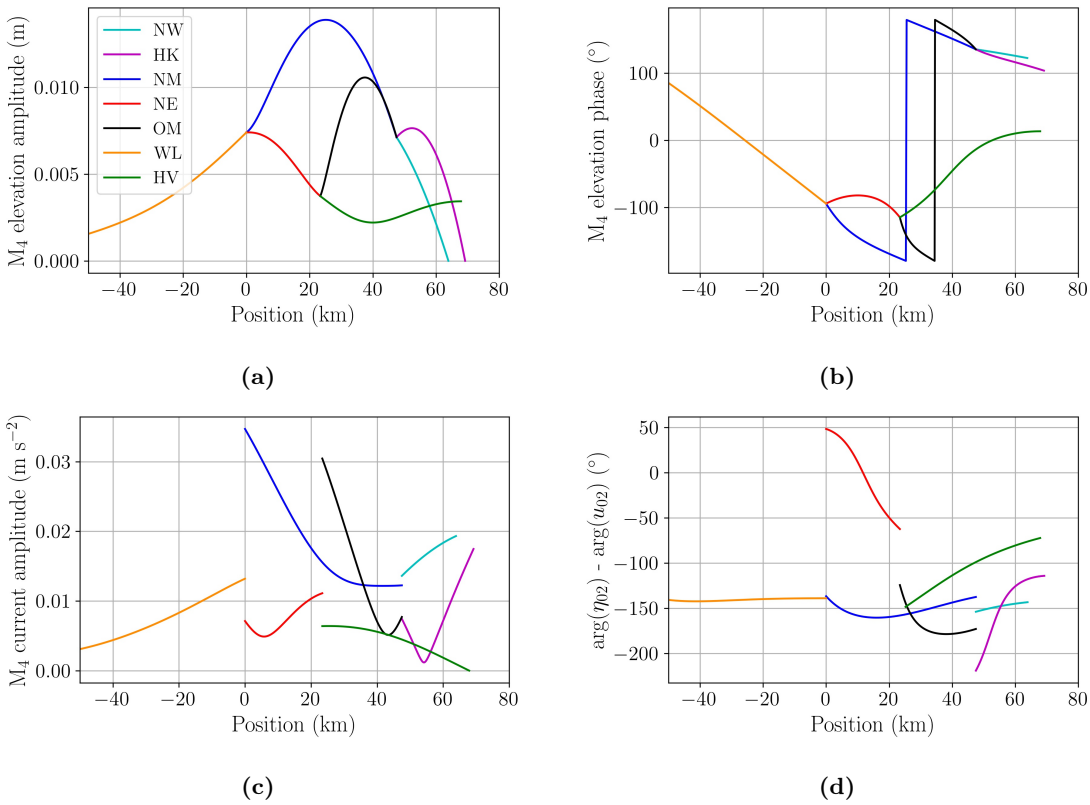

Figure 3.5: a) M_4 elevation amplitudes as a function of position in the Rhine-Meuse network. b) As a), but for elevation phases. c) As a), but for depth-averaged current amplitudes. d) Phase difference between leading order surface amplitude and depth-averaged current velocity.

The M_4 elevation amplitude in Figure 3.5a shows a build-up of M_4 elevation amplitude from the seaward boundary to an approximate local position of 20 km in the network, after which the M_4 elevation amplitude dampens towards the landward boundary. The maximum M_4 elevation amplitude is found in the Nieuwe Maas (NM) with a value of 0.0139 meters. Figure 3.5b shows similar behaviour as was found for the M_2 elevation amplitude, with propagating tidal waves towards the landward boundary in both sea channels and the Nieuwe Maas and Oude Maas (OM). In the Nieuwe Merwede (NE), again a strong reflective wave relative to the incoming wave is found and the phase of the Haringvliet (HV) shows propagating wave behaviour towards the seaward boundary. Figure 3.5c indicates a different distribution for the M_4 current amplitude as was found for the M_2 current amplitude. Both the Nieuwe and Oude Maas

show a strong increase in current amplitude towards the second vertex point. To evaluate which nonlinear contribution dominant is in the Rhine-Meuse and to address the first research question, each of the individual contributions will be shown. Figures 3.6a, 3.6c and 3.6e show respectively the contributions of the return flow due to Stokes drift, no-stress and advection of momentum as a function of the position in the network to the elevation amplitude. Figures 3.6b, 3.6d and 3.6f display the current amplitude of the respective contributions.

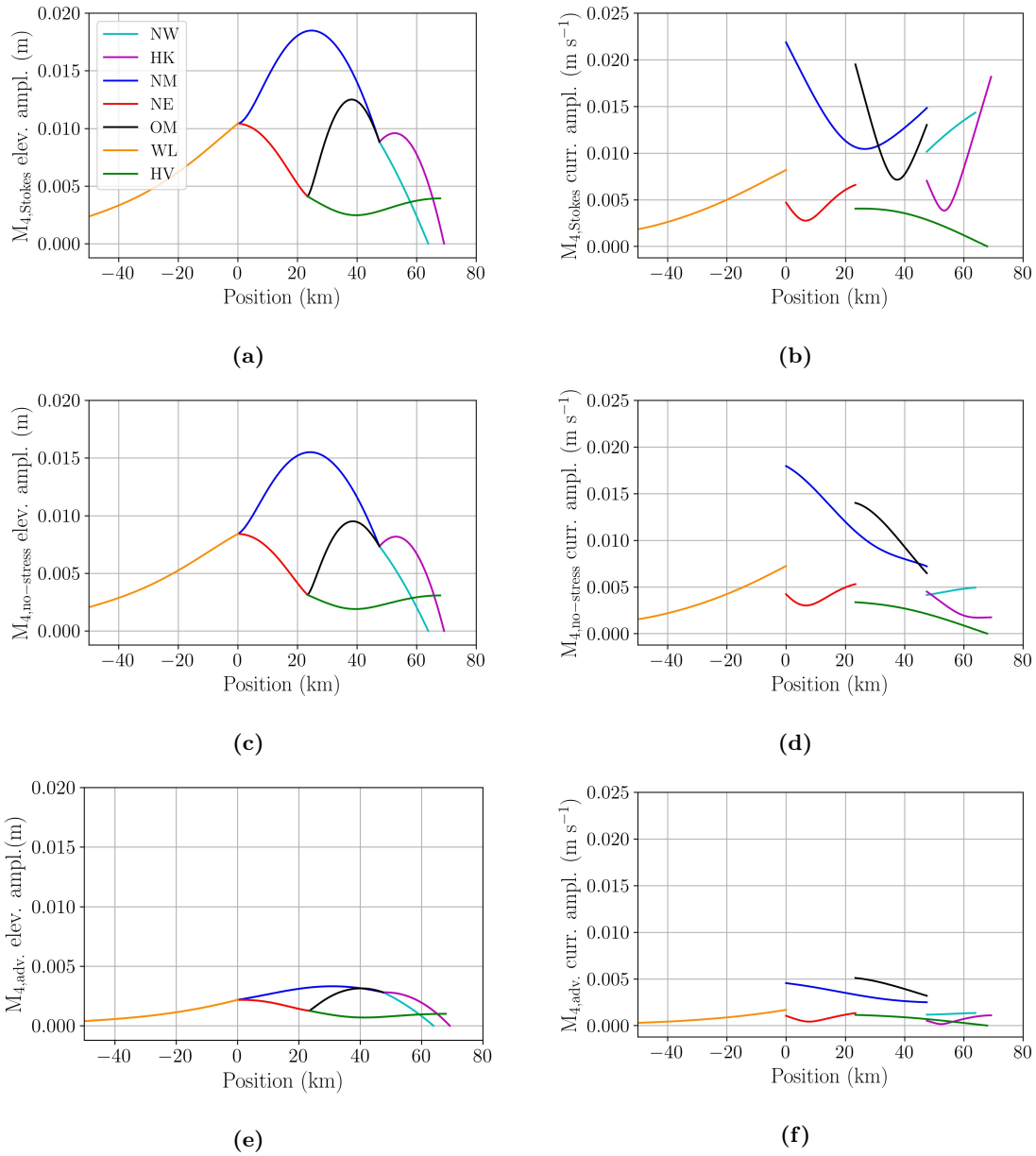

Figure 3.6: a) M_4 elevation amplitudes for the contribution of Stokes as a function of position in the Rhine-Meuse network. b) M_4 current amplitude for the contribution of Stokes as a function of position in the Rhine-Meuse network. c) As a), but for the contribution of the no-stress condition. d) As b), but for the contribution of no-stress condition. e) As a), but for the contribution of advection of momentum. f) As b), but for the contribution of advection of momentum.

Figure 3.6 show that the M_4 amplitudes due to Stokes and no-stress are the most dominant contributions in the network. It is also shown that Stokes and no-stress have a higher maximum than the total internal contribution shown in Figure 3.5a. This can be explained by the phase of the contributions. If one contribution has a phase with the opposite sign compared to the other, dampening of the tidal wave rather than amplifying occurs.

The divergence of excess mass due to Stokes drift is forced by the product between the M_2 elevation and current amplitude and thus strongly dependent on the phase difference between the M_2 elevation and current amplitude. A phase difference of -90° results in transport due to Stokes drift, whereas a phase difference of 0° or -180° results in a maximum return flow. The phase difference between elevation and current is presented in Figure 3.5d. This figure confirms the theory that the divergence of excess mass due to Stokes drift larger is for channels where the phase difference between elevation and current amplitude goes towards -180° or 0°. The current amplitude due to Stokes as shown in Figure 3.6b reveals an inverted pattern relative to the elevation amplitude. The elevation and current amplitude due to the no-stress condition show similar behaviour as for Stokes, as indicated by Figures 3.6c and 3.6d. The no-stress contribution is driven by the product between the M_2 elevation amplitude and the curvature of the M_2 current amplitude and represents the depth-dependent friction. The advection of momentum shows the lowest contribution, as presented in Figures 3.6e and 3.6f. This contribution becomes important when the M_2 current amplitude changes substantially over a relatively small distance.

3.2.3 Externally created M_4 tide

Besides an internally generated M_4 tide, also an externally created M_4 tide is present in the Rhine-Meuse. This external tide has a value of 0.2 meters at the seaward boundaries of both sea channels. The phase difference with the prescribed M_2 tide ($2\phi_{M_2} - \phi_{M_4}$) is 5.4°. The results for the Rhine-Meuse external M_4 elevation amplitudes, elevation phase, depth-averaged current velocity and ratio between internal and external M_4 elevation amplitudes are shown in Figure 3.7.

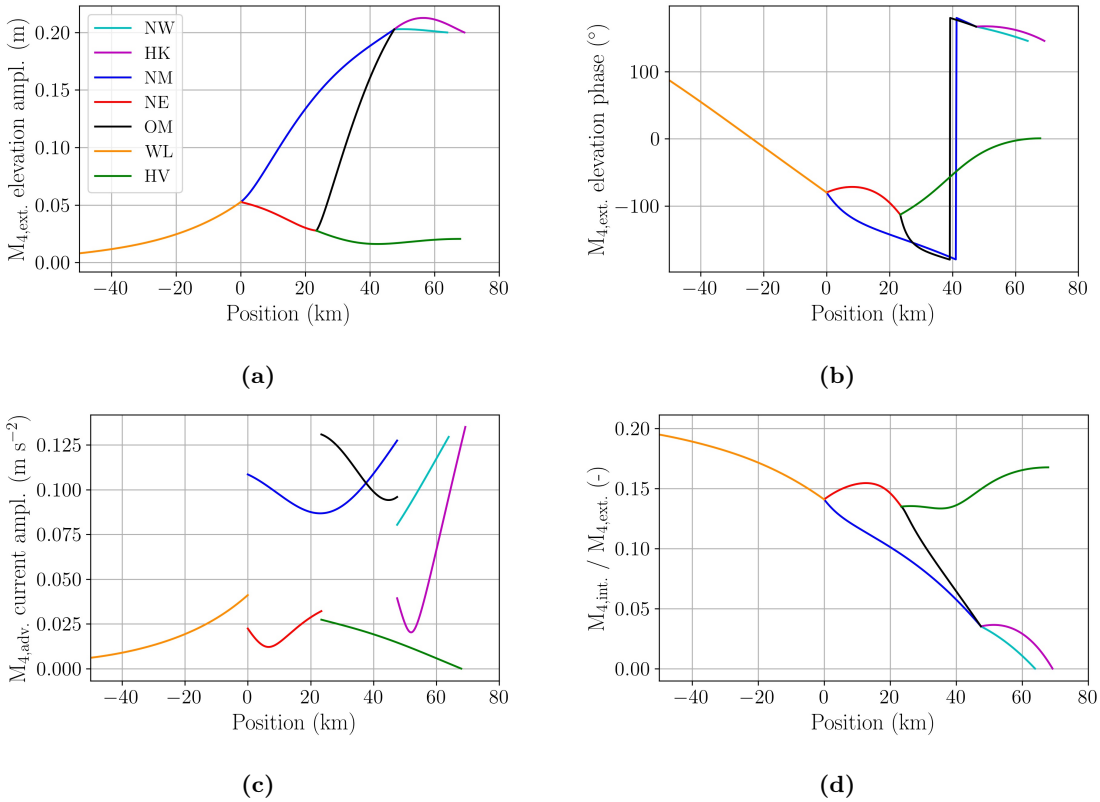

Figure 3.7: a) Externally created M_4 elevation amplitudes as a function of position in the Rhine-Meuse network. b) As a), but for elevation phases. c) As a), but for current amplitudes.

The results in Figure 3.7 indicate similar behaviour as was found for the leading order M_2 elevation and current. The elevation amplitude is about 4 smaller than the M_2 throughout the network. A relatively small difference between both is that in the case of the external M_4 tide amplification of the elevation amplitude occurs for both the sea channels towards the first vertex point. The current amplitude is about 3-5 times smaller than the M_2 current.

Comparing the magnitude of the elevation amplitude for the externally forced M_4 tide with the internally generated M_4 tide in Figure 3.7d, reveals that the externally generated M_4 tide is about 5-15 times larger than the internally generated M_4 tide depending on the position in the network. It is also shown that the relative contribution of the internal tide increases towards the landward boundary, as the principal tide dissipates parts of its energy to the generation of internal higher harmonics.

3.2.4 Full M_4 tide

The total M_4 tide is the sum of the total internally generated tide and externally generated tide. The results for the full elevation and current amplitude, and elevation phase are found in Figure 3.8. For the amplitudes, the results of the harmonic analysis of the measuring stations along the Rhine-Meuse are shown as filled dots in Figure 3.8a.

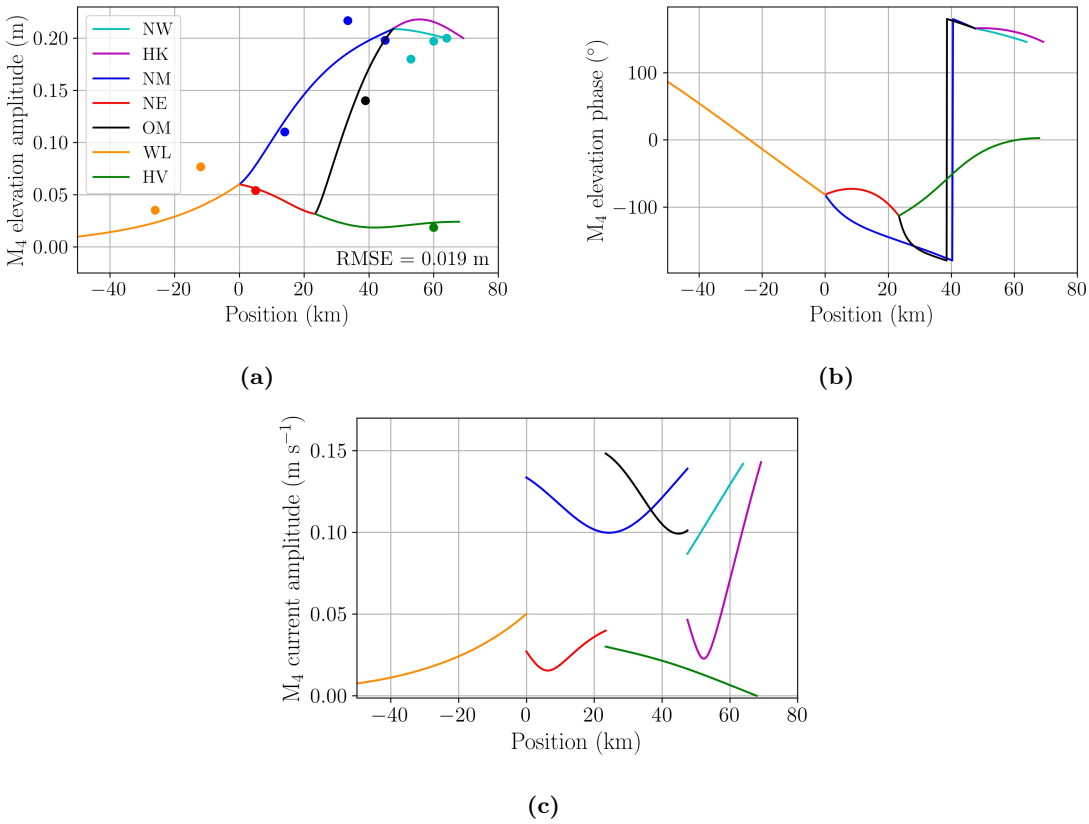

Figure 3.8: a) Full M_4 (internally and externally) elevation amplitudes as a function of position in the Rhine-Meuse network. b) As a), but for elevation phases. c) As a), but for current amplitudes.

Figure 3.8 resembles by a large amount the contribution of the externally prescribed M_4 tide. The internally generated M_4 is only marginally important in the total M_4 contribution in the Rhine-Meuse. Figure 3.8a shows a fair correlation between model and observations, with an RMSE of 0.019 meters. This RMSE is 2.5 times lower in absolute terms than the RMSE for the M_2, however the measurements and model outputs are 4 times lower as well, so the relative error is about 1.5 times higher for the M4 results than for the M_2.

3.2.5 Asymmetry in the Rhine-Meuse

The generation of both the internal and external M_4 has implications for tidal asymmetry as discussed earlier. The four tidal asymmetry quantities for the Rhine-Meuse are shown in Figure 3.9.

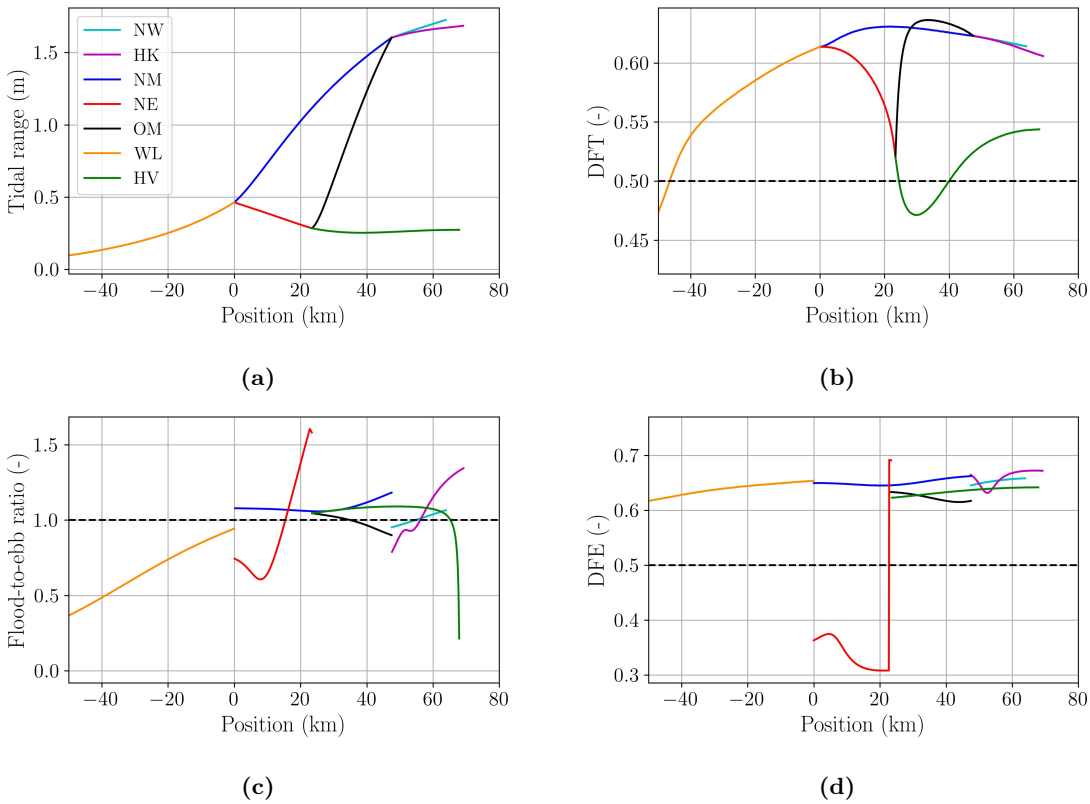

Figure 3.9: a) Tidal range as function of the position in the network for the Rhine-Meuse estuary. b) As a), but for DFT. c) As a), but for Flood-to-ebb ratio. d) As a, but for DFE.

The tidal range in Figure 3.9a reveals the pattern of the M_2 and external M_4 elevation amplitude, with a dampening of the tidal range towards the landward boundary. Figure 3.9b shows the DFT in the network. This figure illustrates flood dominant behaviour throughout most of the network. Meaning the tide travels faster in the flood phase than in the ebb phase. However, as the influence of tides on the landward side decreases, flood dominant behaviour also decreases and a shift to ebb dominance is observed at the further end of the river. Also, the Haringvliet (HV) shows for a short distance ebb dominant behaviour. The flood-to-ebb ratio in Figure 3.9c reveals a mix of ebb dominance and flood dominance for most of the channels. The river channel the Waal (WL) indicates an increase in ebb dominance towards the landward boundary. This can be related to the relatively strong river velocity and diminishing tides in this channel. The sharp transition to ebb dominant behaviour for the Haringvliet can be explained by the fact that the tidal current velocities go to zero at the seaward boundary, while a river velocity greater than zero does exist at these locations. This favours ebb dominant behaviour for the current velocities. Figure 3.9d shows flood dominant behaviour in most of the network, meaning that the transition from flood to ebb takes more time than the transition from ebb to flood.

Concerning the relation with sediment transport, these result would imply that the transport of suspended sediments occurs in landwards in the Rhine-Meuse. For bedload transport different behaviour would occur. The presence of a relatively strong river velocity in the river

channel indicates seaward bedload transport of sediments. This is also the case for part of the Nieuwe Merwede, Haringvliet and Oude Maas. The other channels reveal landward transport. The change from flood dominance to ebb dominance for DFE in the Nieuwe Merwede results from two low water peaks in the ebb phase consisting of two maxima separated by a small depression in the current velocity, also called double tide. This behaviour and the shift from flood dominant to ebb dominant is shown in Figure 3.10.

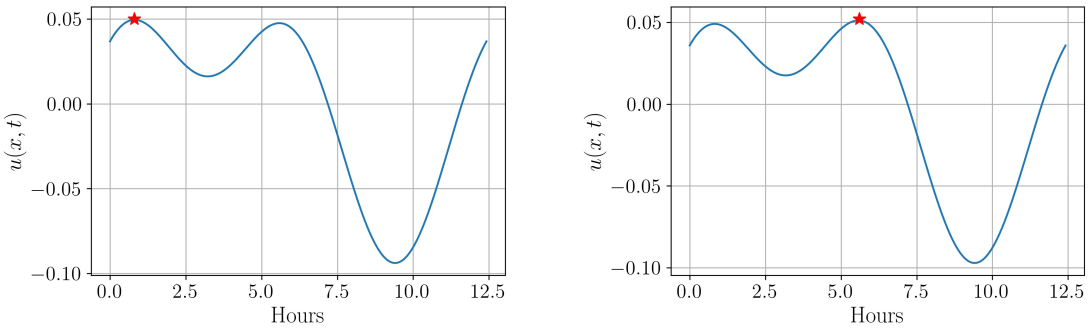

(a) **(b)**

Figure 3.10: a) Current velocity as a function of time for the Nieuwe Merwede (NE) in the case of ebb dominance. b) As a) but for flood dominance. The red star indicates the highest ebb peak. Note: positive currents mean ebb phase, negative currents mean flood phase.

As was indicated by Figure 3.4, large gradients in the current amplitude over the vertical distance occur in this system. Therefore, it is important to examine the degree of asymmetry in the current amplitude as a function of the depth of the channels. This has been done for two channels, namely the Nieuwe Waterweg and Nieuwe Maas. Both velocity asymmetry (DFE) and flood-to-ebb ratio on both channels are investigated. The results are shown in Figure 3.11. The upper two panels indicate the degree of velocity asymmetry (DFE) in both the channels. These reveal that the DFE is slightly larger near the bottom of the channels than near the surface. For the flood-to-ebb ratio in the lower two figures, an inverse pattern is shown. The largest values for the flood-to-ebb ratio appear to be near the surface of the channels and a decrease in magnitude is found deeper in the channel.

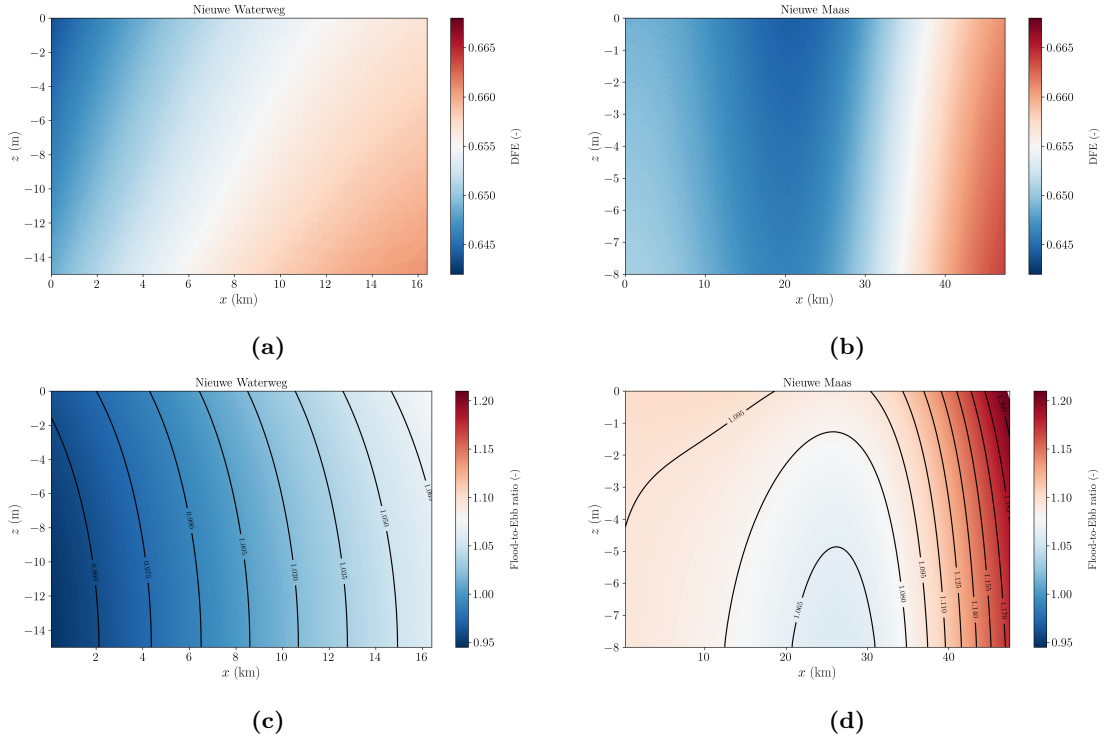

Figure 3.11: a) DFE as a function of x and z for the Nieuwe Waterweg b) As a), but for Nieuwe Maas. c) Flood-to-ebb ratio as a function of x and z for the Nieuwe Waterweg d) As c), but for Nieuwe Maas.

3.3 Opening of one of the Haringvliet sluices

The difference in M_2 and M_4 sea surface elevation, elevation phase, depth-averaged current amplitude and velocity phase between an open and closed scenario of the Haringvliet sluice is shown in Figures 3.12.

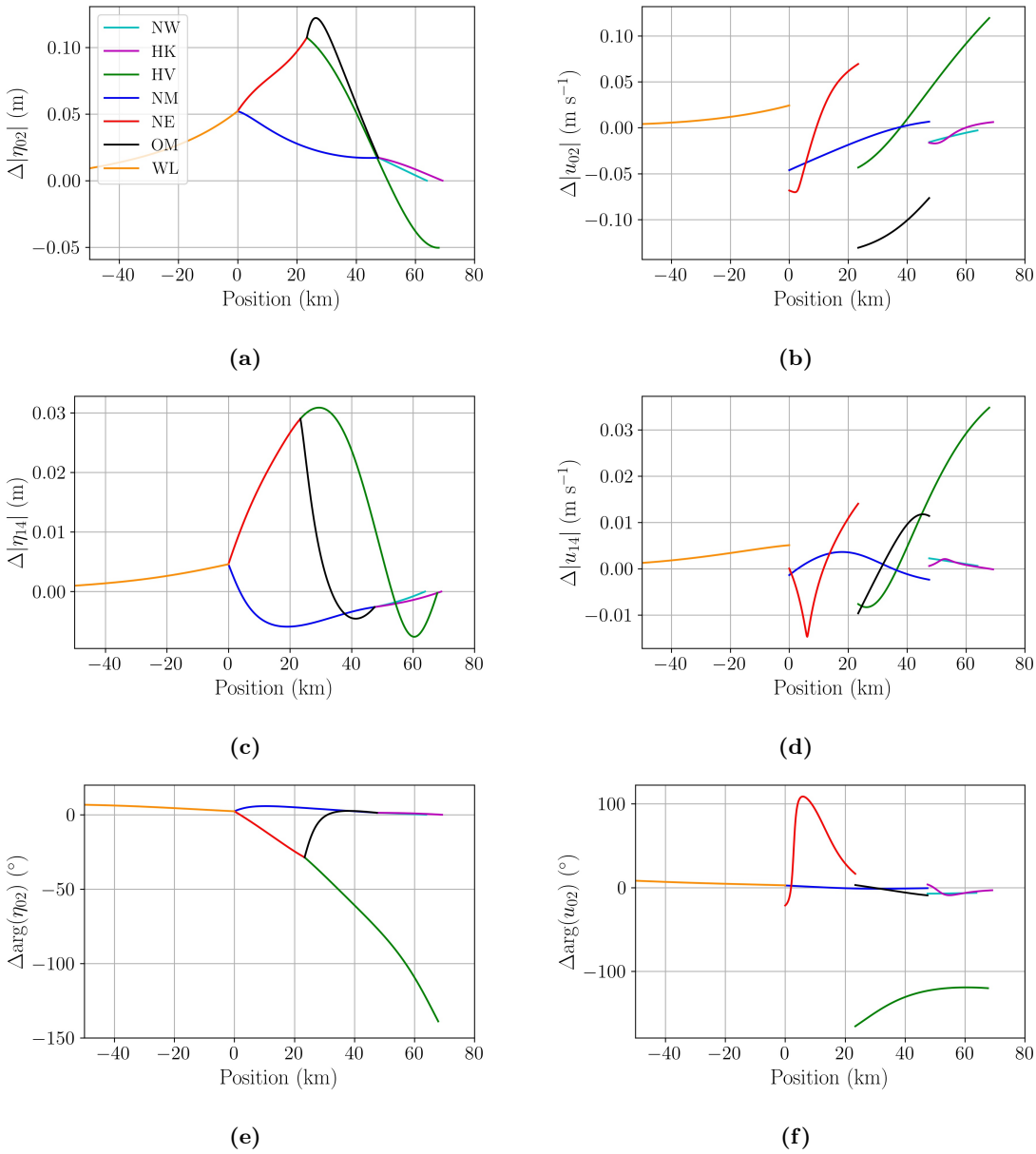

Figure 3.12: a) Difference in M_2 elevation amplitudes between opening of the Haringvliet sluice and closed as a function of position in the Rhine-Meuse network. b) As a), but for M_2 depth-averaged current amplitudes. c) As a), but for M_4 elevation amplitudes. d) As a), but for M_4 depth-averaged current amplitudes. e) As a), but for M_2 elevation phase. f) As a), but for M_2 depth-averaged current phase.

Figure 3.12a indicates a maximum increase in M_2 elevation amplitude of 11.6 cm due to the opening of one of the sluices of the Haringvliet. The vertex point at around 20 km shows the highest increase in amplitude. This is as expected since the Haringvliet branches at this vertex point. This results in a propagating tidal wave in the direction of the vertex point after the opening, instead of a propagating wave in the direction of the boundary of the Haringvliet. The initial decrease in amplitude in the Haringvliet after opening, compared with closed, can possibly be explained by a stronger reflective wave in the case of the fully closed Haringvliet. The M_4 elevation amplitude shows a similar pattern of increase, with especially an increase at the vertex point at around 20 km. The maximum increase in M_4 elevation amplitude is 3.0 cm and can mainly be contributed due to an increase in external M_4. For the current amplitudes at Figure 3.12b and 3.12d, a mix of both increases an decreases appear. The largest increase in both M_2 and M_4 current amplitude is found at the entrance of the Haringvliet, with respectively an increase of 0.123 and 0.034 $\mathrm{m\,s^{-1}}$. In the Oude Maas (OM) an decrease in M_2 current amplitude was found of around 25%, compared to a closed Haringvliet. This decrease is partly compensated at the vertex points at around 20 km. At this location, the Nieuwe Merwede (NE) shows a strong increase in current velocity. Figure 3.12e indicates strong changes in the propagating behaviour of the M_2 tide in the network. The Haringvliet demonstrates the largest difference, with now a propagating wave landward. Furthermore, the strong propagating wave in the Oude Maas in the closed scenario decreased by a fair amount with the opened scenario. Also, the standing wave behaviour that was found in the Nieuwe Merwede now transformed to a fully propagating wave landward. Lastly, the difference in M_2 current amplitude phase in Figure 3.12f shows especially large differences over distance in the Nieuwe Merwede.

3.4 Influence of sea level rise (SLR)

The difference in M_2 and M_4 sea surface elevation, elevation phase, depth averaged current amplitude and velocity phase between current and SLR conditions is presented in Figure 3.12.

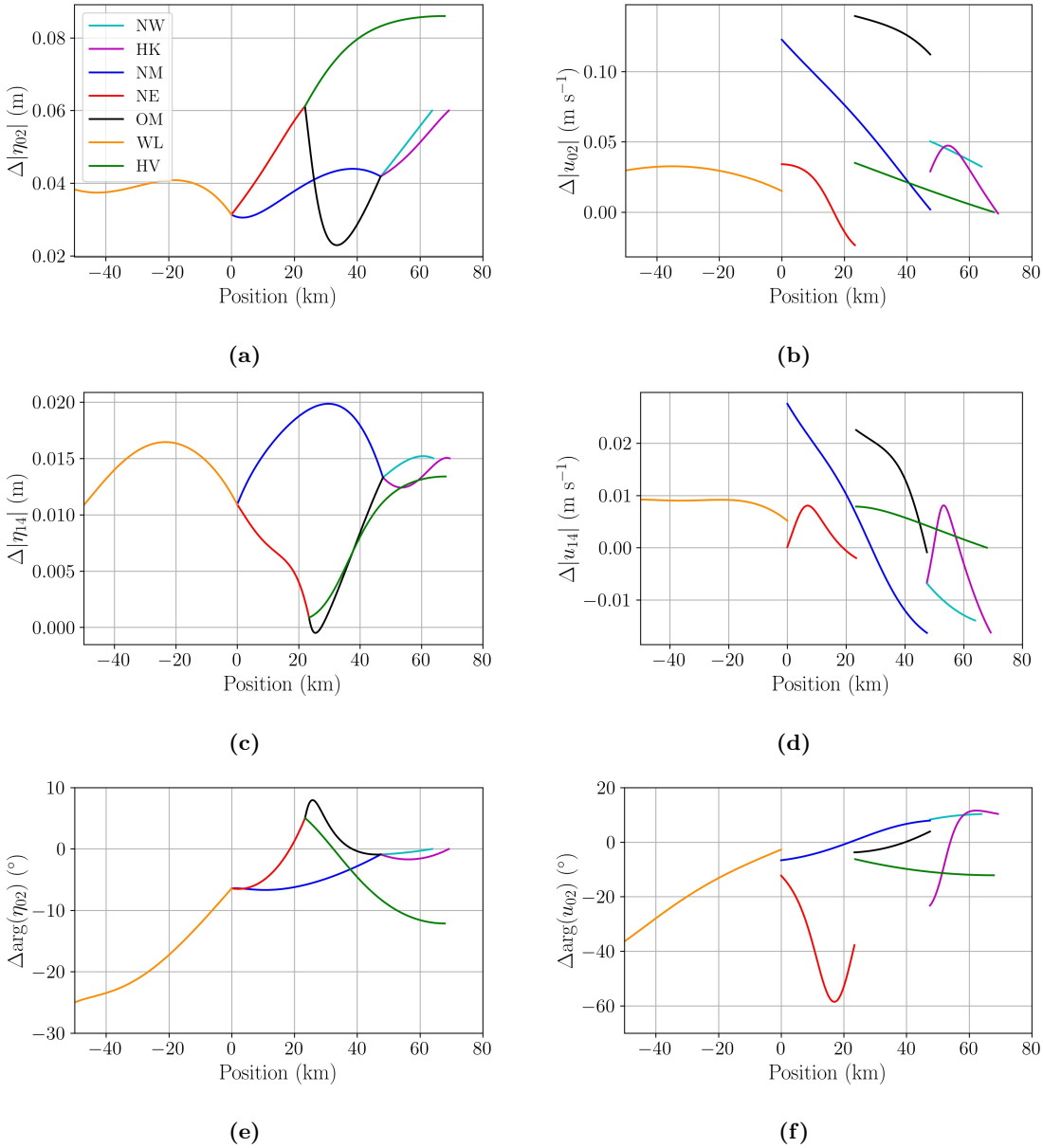

Figure 3.13: a) Difference in M_2 elevation amplitudes between SLR conditions and current conditions as a function of position in the Rhine-Meuse network. b) As a), but for M_2 depth-averaged current amplitudes. c) As a), but for M_4 elevation amplitudes. d) As a), but for M_4 depth-averaged current amplitudes. e) As a), but for M_2 elevation phase. f) As a), but for M_2 depth-averaged current phase.

Figure 3.13a shows that the impact of SLR on the M_2 elevation amplitude relatively low is. The largest differences can be found in the Haringvliet (HV) with an increase of around 8 cm. However, that is still a marginal increase, considering the 2-meter SLR in every channel. In general, making channels deeper can be expected to reduce tidal dampening by lowering the experience of bottom friction. Thus, the relative impact of SLR on reducing bottom friction will be experienced most strongly in the shallower channels. However, internal friction is parameterised with channel depth. This implies that internal friction increases with channel depth. And so, this effect acts inversely to the decrease in bottom friction on the tide. Figure 3.13c demonstrates a different pattern than was found for the M_2 elevation amplitude. However, it shows similarities with the pattern found for the total internal M_4 tide without SLR. This reveals that, in this scenario, the increase in the internally generated M_4 tide is stronger than in the scenario with the opening of the Haringvliet sluice. The difference in M_2 current amplitude in Figure 3.13b generally shows an increase in M_2 current amplitude. The current now feels less friction compared to the case with the more shallow channels and thus less dampening occurs. The largest current amplitude increase is found in the Nieuwe Maas, with an increase of around 25% compared to the current conditions. For the M_4 current amplitude in Figure 3.13d, relatively less increase is found compared to the M_2 current amplitude. Here, most channels show a combination of increased and decreased current amplitudes or even completely decreased. The elevation phase in Figure 3.13e indicates an overall decrease in the phase speed compared to the current conditions for most of the channels. The Nieuwe Maas, however, shows an even stronger propagating wave landward in this scenario. The Nieuwe Merwede reveals now propagating behaviour in the seaward direction, due to the presence of an even more dominant reflective wave in this scenario. Large differences are also found for the phase of the M_2 current amplitude in Figure 3.13f. In most channels a decrease in phase in the landward direction occurs. The Nieuwe Merwede again reveals large differences over distance in the current amplitude phase.

4 | Discussion

4.1 General

This study builds on previous work by Wang et al. (2021) with the addition of incorporating the nonlinear tides in estuarine networks. An idealised model that allows for semi-analytical solutions have been used here to gain an understanding of the hydrodynamics of these systems. A different modelling approach would be by developing a numerical model. The difference between a numerical model and an idealised model is that an idealised model only takes the processes into account that are necessary to study the subject of choice (Murray, 2003). This simplified approach makes it convenient to investigate individual processes in detail and to compare their relative importance to each other. Because of its simplicity, an accurate representation cannot be obtained as easily as with a numerical model. The complexity of numerical models makes them better suited for quantitative research. On the other hand, it is more difficult to investigate the individual processes with a numerical model separately. The features of both types of models can reinforce each other by, for example, using an idealised model to first gain insight into the dominant processes within an estuary and then subsequently applying this knowledge in a numerical model. The results show that the model has been successfully applied to a three-channel network, with findings in agreement with Wang et al. (2022). In addition, application of the model to the Rhine-Meuse has also proven successful when a comparison is made with observations from monitoring stations. The correlation between model results and observations for the Rhine-Meuse is shown in Figure 4.1.

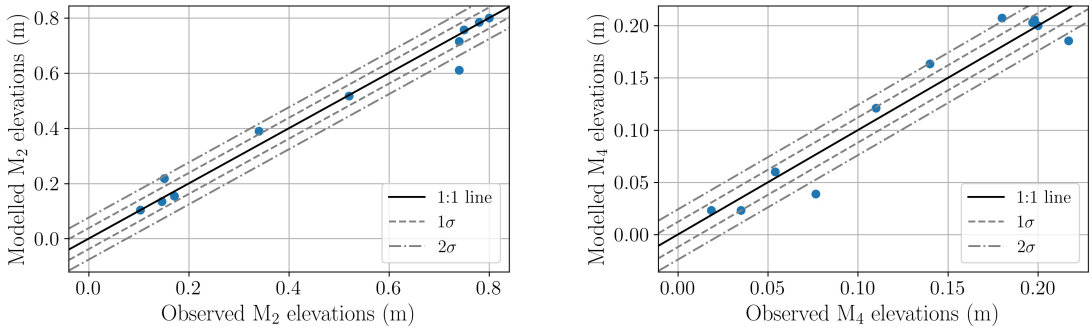

(a) **(b)**

Figure 4.1: a) Modelled M_2 elevation amplitudes as a function of observed amplitudes for the case in which the RMSE is minimized. Black line represent the 1:1 ratio fit between modelled and observed. The dotted and dashed dotted lines are respectively the 1σ and 2σ confidence intervals. b) As a), but for modelled M_4 elevation amplitudes.

The standard deviation represents the spread in absolute error between model and observation. This shows that a larger standard deviation is found for the M_4 tide, compared to the M_2 tide. Furthermore, Figure 4.1a shows that most of the points fall within the 1σ confidence interval for the M_2 tide. Only one point falls outside of the 2σ confidence interval. The results for the M_4 in Figure 4.1b show more spread, with still most of the points within the 2σ confidence interval and two points outside of the 2σ confidence interval. With regards to the river flow in the Rhine-Meuse, the distribution of river discharge indicated that the Nieuwe Waterweg discharges the largest part, followed by the Haringvliet. This was also found by Cox et al. (2021). However, they did find an even larger contribution for the Nieuwe Waterweg. This difference can be explained by the fact that the 'Spui' passage was not included in the current study. This passage displaces approximately 20% of the total discharge from the Haringvliet to the Nieuwe Waterweg, according to Cox et al. (2021).

The importance of a 2DV modelling approach was demonstrated for velocity asymmetry and flood-to-ebb ratio. Velocity asymmetry (DFE) revealed an increase in asymmetry towards the bottom of the channels. For the flood-to-ebb ratio, the opposite was found. Flood-to-ebb ratio is particularly known for bedload transport of sediment, as was show by Aubrey (1986). An overestimation of the flood-to-ebb ratio would have been discovered if a 1D model, which only takes the surface current into account, or if a depth-averaged current had been used to quantify the degree of asymmetry in peak flood and ebb current.

It should be noted that Rhine-Meuse is probably not comparable for most systems in the world. Due to the geometrical proportions of the North Sea, a strong external M_4 tide is present in this network. Thus, the total M_4 (the sum of internal plus external) is dominated by the external M_4. This implies that just by resolving the external M_4 in this network, a relatively good estimate can already be made for the total M_4 tide without considering the internal processes.

4.2 Decisions and assumptions in the model

During the process of developing an idealised model, decisions and assumptions are made that simplify certain processes and neglect others. Some of those will be discussed in this section.

4.2.1 Model framework

When constructing a 2DV model, negligible variations in the lateral direction in the estuary are assumed. In reality, lateral currents are present in estuaries, as shown analytically and numerically by studies such as Huijts et al. (2009); Scully et al. (2009). A more accurate representation here would be a 3D framework, however, this complicates the model drastically. Furthermore, in reality, there are variations in the depth of each channel over distance. For example, a channel may have a sloping bottom towards or away from a vertex point. Accounting for these variations in depth will also result in a more even transition between channels at vertex points with less discontinuity in current velocities at these positions. However, including depth variations in the model results in extra terms in the ODE for the waterlevel due to the fact that H is now differentiable in x.

An simplified representation of the Rhine-Meuse has been used with three vertex points. In actuality, there are still a number of other small passages and channels in the network that

lead to additional vertex points. However, it was found in this study, that not including some small channels did not have a major impact on the overall hydrodynamics in the network when looking at the correlation with observations. This consideration is strengthened by the role of the Nieuwe Merwede in the network. This channel acts as a passage between two vertex points and shows relatively little change over distance for both the elevation amplitude as well as the current velocity. An inference based on this observation would be, for example, that it is pointless to build a dam in this channel considering the role of the tides here.

Bottom friction and turbulence are parameterized with constant values per channel. In reality, the value of these friction parameters are different for each location in the horizontal direction. Besides, eddy viscosity is also variable in the vertical direction and typically expressed as a parabolic function, for instance, Burchard and Hetland (2010); Zitman and Schuttelaars (2012) have studied this. This allows the vertical structure of the current velocity and thereby tidal asymmetry to be modelled more accurately. Additionally, eddy viscosity is time dependent due to varying current velocities between flood and ebb. A_v is generally larger during flood than during ebb because of tidal straining (Simpson et al., 1990).

The influence of wind on tides was not included in this study. However, this does influence the tides locally. For example, an inland wind parallel to the horizontal direction in a certain channel exaggerates high tide and attenuates low tide. Additionally, wind straining in estuaries can be important for estuarine circulation, as was found by Lange and Burchard (2019). Furthermore, this research focuses on the time-dependent part of Stokes, no-stress and advection were examined. As was shown earlier in this report, also a time-independent part, a so-called residual flow, of these processes exists. This residual flow is especially important in the context of circulation patterns when considering the behaviour of the system for periods longer than one tidal cycle.

4.2.2 Nonlinear processes

In addition to decisions in the framework of the model, there are several processes not included in this study that generate overtides in estuaries. This concerns, for example, the already mentioned transverse currents can also provide nonlinear tide generation, in the form of a transverse contribution to the advection of momentum, as shown by Huijts et al. (2009). Also, temporal variations in eddy viscosity during a tidal cycle results in tidal and gravitational eddy viscosity-shear covariance circulation (ESCO), causing interactions between M_2 tidal flow and M_2 eddy viscosity (Dijkstra et al., 2017b). These processes are not addressed if an eddy viscosity constant in time is used. Furthermore, an estuary is stratified with layers of different densities. This stratification is particularly driven by salt and temperature differences that can be modelled by adding a baroclinic pressure term to the momentum equation, in addition to the static pressure term. This results in a nonlinear contribution due to baroclinic pressure, shown in, for example, Dijkstra et al. (2017a). Moreover, tidal flats are also known to be a source of nonlinear tides. Typically ebb dominance occurs when tidal flats are flooded during high tide and subsequently release this water during low tide (see: Speer and Aubrey (1985); Friedrichs and Aubrey (1994)). Additionally, tidal flats can act as momentum sinks, as shown by Alebregtse et al. (2012). Lastly, on this topic, the earlier mentioned river-tide interaction has not been evaluated in this study. The river-tide interaction can be modelled through the bottom stress, which is in this current study linearised. However, solving for each harmonic

component result in tidal distortion, as proven by Godin (1999).

4.3 Further work

This study demonstrated that a 2DV idealised model is capable of achieving meaningful results for both linear and non-linear tides. The Rhine-Meuse is identified as a flood dominant system. For future research, it is valuable to also test this identification in a sediment dynamics model. Also, in view of the SALTI-solutions project, this model can be further extended to study other ecological applications, such as phytoplankton or salt. The model has also been shown to be useful for studying scenarios. For follow-up research related to water management, the influence of, for instance, deepening or closing specific channels can be studied. Some model choices and assumptions were explained in the previous subsection. Follow-up research can reveal the exact influence of these assumptions and identify which sources of non-linearity are relevant for this system. The most logical extension is an improved turbulence model, in which the friction parameters include the various harmonic components and the river-tide interaction, allowing this model to be applied accurately to systems with few or no monitoring stations.

5 | Conclusions

This study concerns identifying the dominant internal mechanisms that contribute to the internal generation of the M_4 tide and subsequently examining how this internally generated M_4 tide compares to the externally forced M_4 tide in rhw estuarine network. In doing so, the type of tidal asymmetry resulting from the presence of these overtides in the system was also investigated.

To study this, a 2DV semi-analytical idealized model was developed that allows for individual contributions to be easily examined and sensitivity studies to be quickly applied. Two networks were examined here: an idealized three-channel network and the Rhine-Meuse estuarine network. The chosen research questions are being addressed on the Rhine-Meuse network. The findings show that for both systems, the model produces results for both the M_2 and the M_4 are consistent with previous research or observations.

To address the first research question, the internal mechanisms causing internally generated M_4 tide has been examined separately in the Rhine-Meuse. This revealed that the divergence of excess mass due to Stokes drift and then followed by the no-stress condition make the largest contribution to the total internally generated M_4 tide. Advection of horizontal momentum was overall of less importance in this network.

To address the second research question, the externally forced M_4 tide was determined and compared to the internally generated M_4 tide in the Rhine-Meuse network. Results showed that the elevation amplitude for this external tide is a factor 5-15 times larger than the elevation amplitude of the internally generated M_4 tide depending on the position in the network. The current amplitude of the externally forced M_4 tide was found to be a factor 3-5 times larger than the internally generated M_4 current amplitude.

To address the third research question, in the Rhine-Meuse network, flood dominant behavior has been found as a consequence of the presence of overtides. Velocity and duration asymmetry in this system have both been shown to be equally dominant in the upper part of the estuary. However, a decrease in flood dominant duration asymmetry is observed as the tide moves further inland. The flood-to-ebb ratio reveals both ebb and flood dominant behavior. It is further shown that velocity asymmetry becomes more dominant lower in the water column and flood-to-ebb ratio demonstrated higher values near the surface than near the bottom. These findings demonstrate the importance of a 2DV model.

To address the fourth research question, the opening of one of the Haringvliet sluices during flood and sea level rise have been conducted as sensitivity studies on the Rhine-Meuse network. The results of opening one of the sluices shows a sharp increase in M_2 and M_4 elevation amplitude especially in the Haringvliet and Oude Maas, with maximum increases of 11.6 and 3.0 cm, respectively. The M_2 and M_4 current velocities reveal a mix of increases

and decreases at opening. Here the increase and decrease for the vast majority of the system is ± 0.10 m s^{-1} for the M_2 and 0.01 m s^{-1} for the M_4. A sea level rise of 2 meters in the Rhine-Meuse leads to a maximum increase of 0.04 m/m SLR and 0.01 m/m SLR for the M_2 and M_4 elevation amplitude, respectively. For the M_2 current amplitude an increase was found overall, with maximum value of 0.06 m s^{-1}/m SLR. The M_4 current amplitude shows increases and decreases in the range of ± 0.01 m s^{-1}/m SLR. Furthermore, the results indicated that opening of the one of the Haringvliet sluices generally increases the phase speed of the M_2 tide in the landward direction and a decrease of phase speed, on the other hand, was found for the scenario of 2-meter SLR.

Bibliography

Alebregtse, N. and De Swart, H. (2014). Effect of a secondary channel on the non-linear tidal dynamics in a semi-enclosed channel: a simple model. *Ocean dynamics*, 64(4):573–585.

Alebregtse, N. and de Swart, H. (2016). Effect of river discharge and geometry on tides and net water transport in an estuarine network, an idealized model applied to the Yangtze Estuary. *Continental Shelf Research*, 123:29–49.

Alebregtse, N., De Swart, H., and Zimmerman, J. (2012). Tidal asymmetries in estuaries due to channel-flat interactions, a simple model. *Proc., NCK-days 2012: Crossing borders in coastal research*.

Aubrey, D. (1986). Hydrodynamic controls on sediment transport in well-mixed bays and estuaries. *Physics of shallow estuaries and bays*, 16:245–258.

Burchard, H. and Hetland, R. D. (2010). Quantifying the contributions of tidal straining and gravitational circulation to residual circulation in periodically stratified tidal estuaries. *Journal of Physical Oceanography*, 40(6):1243–1262.

Buschman, F., Hoitink, A., van der Vegt, M., and Hoekstra, P. (2010). Subtidal flow division at a shallow tidal junction. *Water Resources Research*, 46(12).

Cameron, W. and Pritchard, D. (1963). Estuaries. *The Sea*. pages 306–324.

Cox, J. R., Huismans, Y., Knaake, S., Leuven, J., Vellinga, N., van der Vegt, M., Hoitink, A., and Kleinhans, M. (2021). Anthropogenic effects on the contemporary sediment budget of the lower rhine-meuse delta channel network. *Earth's Future*, 9(7):e2020EF001869.

Csanady, G. T. (1981). Circulation in the coastal ocean. In *Advances in geophysics*, volume 23, pages 101–183. Elsevier.

Defant, A. (1961). *Physical Oceanography*. Pergamon Press.

Dijkstra, Y. M., Brouwer, R. L., Schuttelaars, H. M., and Schramkowski, G. P. (2017a). The iflow modelling framework v2. 4: A modular idealized process-based model for flow and transport in estuaries. *Geoscientific Model Development*, 10(7):2691–2713.

Dijkstra, Y. M., Schuttelaars, H. M., and Burchard, H. (2017b). Generation of exchange flows in estuaries by tidal and gravitational eddy viscosity-shear covariance (ESCO). *Journal of Geophysical Research: Oceans*, 122(5):4217–4237.

Dronkers, J. (1986). Tidal asymmetry and estuarine morphology. *Netherlands Journal of Sea Research*, 20(2-3):117–131.

Dronkers, J. J., Schönfeld, J., and Waalewijn, A. (1959). Tidal computations in shallow water-report on hydrostatic levelling across the westerschelde. *Rijkswaterstaat Communications 01*.

Friedrichs, C. T. (2010). Barotropic tides in channelized estuaries. *Contemporary issues in estuarine physics*, 27:61.

Friedrichs, C. T. and Aubrey, D. G. (1988). Non-linear tidal distortion in shallow well-mixed estuaries: a synthesis. *Estuarine, Coastal and Shelf Science*, 27(5):521–545.

Friedrichs, C. T. and Aubrey, D. G. (1994). Tidal propagation in strongly convergent channels. *Journal of Geophysical Research: Oceans*, 99(C2):3321–3336.

Geyer, W. R. and MacCready, P. (2014). The estuarine circulation. *Annu. Rev. Fluid Mech*, 46(1):175–197.

Godin, G. (1999). The propagation of tides up rivers with special considerations on the upper Saint Lawrence River. *Estuarine, Coastal and Shelf Science*, 48(3):307–324.

Groen, P. (1967). On the residual transport of suspended matter by an alternating tidal current. *Netherlands Journal of Sea Research*, 3(4):564–574.

Hill, A. and Souza, A. (2006). Tidal dynamics in channels: 2. Complex channel networks. *Journal of Geophysical Research: Oceans*, 111(C11).

Huijts, K., Schuttelaars, H., De Swart, H., and Friedrichs, C. (2009). Analytical study of the transverse distribution of along-channel and transverse residual flows in tidal estuaries. *Continental Shelf Research*, 29(1):89–100.

Ianniello, J. (1977). Tidally induced residual currents in estuaries of constant breadth and depth. *Journal of Marine Research*, 35:755–786.

Ianniello, J. P. (1979). Tidally induced residual currents in estuaries of variable breadth and depth. *Journal of Physical Oceanography*, 9(5):962–974.

Lange, X. and Burchard, H. (2019). The relative importance of wind straining and gravitational forcing in driving exchange flows in tidally energetic estuaries. *Journal of Physical Oceanography*, 49(3):723–736.

Lorentz, H. (1926). Verslag van de Staatscommissie Zuiderzee. *Algemene Landsdrukkerij,'s-Gravenhage*.

Murray, A. B. (2003). Contrasting the goals, strategies, and predictions associated with simplified numerical models and detailed simulations. *Geophysical Monograph-American Geophysical Union*, 135:151–168.

Oppenheimer, M., Glavovic, B., Hinkel, J., van de Wal, R., Magnan, A. K., Abd-Elgawad, A., Cai, R., Cifuentes-Jara, M., Deconto, R. M., Ghosh, T., et al. (2019). Sea level rise and implications for low lying islands, coasts and communities.

Parker, B. B. (1991). The relative importance of the various nonlinear mechanisms in a wide range of tidal interactions. *Tidal hydrodynamics*, 13:237–268.

Pawlowicz, R., Beardsley, B., and Lentz, S. (2002). Classical tidal harmonic analysis including error estimates in MATLAB using T-TIDE. *Computers & Geosciences*, 28(8):929–937.

Pfeffer, W. T., Harper, J. T., and O'Neel, S. (2008). Kinematic constraints on glacier contributions to 21st-century sea-level rise. *Science*, 321(5894):1340–1343.

Pickering, M. D., Wells, N., Horsburgh, K., and Green, J. (2012). The impact of future sea-level rise on the European Shelf tides. *Continental Shelf Research*, 35:1–15.

Pietrzak, JD (2019). Salti-solutions. `https://kbase.ncr-web.org/saltisolutions/,Lastaccessedon2022-10-12`,.

Prandle, D. (1997). The influence of bed friction and vertical eddy viscosity on tidal propagation. *Continental Shelf Research*, 17(11):1367–1374.

Rijkswaterstaat (2022a). Millingen a/d Rijn debiet. `https://waterinfo.rws.nl/#!/details/publiek/waterafvoer/Millingen-ad-Rijn(MILL)/Debiet___20Oppervlaktewater___20m3___2Fs,Lastaccessedon2022-10-05`,.

Rijkswaterstaat (2022b). Water level Rhine-Meuse. `https://waterinfo.rws.nl/#!/kaart/waterhoogte/,Lastaccessedon2022-09-15`,.

Sassi, M. G., Hoitink, A., De Brye, B., Vermeulen, B., and Deleersnijder, E. (2011). Tidal impact on the division of river discharge over distributary channels in the Mahakam Delta. *Ocean Dynamics*, 61(12):2211–2228.

Scully, M. E., Geyer, W. R., and Lerczak, J. A. (2009). The influence of lateral advection on the residual estuarine circulation: A numerical modeling study of the Hudson River estuary. *Journal of Physical Oceanography*, 39(1):107–124.

Simpson, J. H., Brown, J., Matthews, J., and Allen, G. (1990). Tidal straining, density currents, and stirring in the control of estuarine stratification. *Estuaries*, 13(2):125–132.

Song, D., Wang, X. H., Kiss, A. E., and Bao, X. (2011). The contribution to tidal asymmetry by different combinations of tidal constituents. *Journal of Geophysical Research: Oceans*, 116(C12).

Speer, P. and Aubrey, D. (1985). A study of non-linear tidal propagation in shallow inlet/estuarine systems part ii: Theory. *Estuarine, Coastal and Shelf Science*, 21(2):207–224.

Valle-Levinson, A. (2010). Definition and classification of estuaries. *Contemporary issues in estuarine physics*, 1:1–10.

Van Wijngaarden, M. (1999). A two-dimensional model for suspended sediment transport in the southern branch of the Rhine–Meuse estuary, the Netherlands. *Earth Surface Processes and Landforms: The Journal of the British Geomorphological Research Group*, 24(13):1173–1188.

Vellinga, P., Katsman, C., Sterl, A., Beersma, J., Hazeleger, W., Church, J., Kopp, R., Kroon, D., Oppenheimer, M., Plag, H.-P., et al. (2009). Exploring high-end climate change scenarios for flood protection of the Netherlands. Technical report, KNMI.

Wang, J., De Swart, H. E., and Dijkstra, Y. M. (2021). Dependence of tides and river water transport in an estuarine network on river discharge, tidal forcing, geometry and sea level rise. *Continental Shelf Research*, 225:104476.

Wang, J., Dijkstra, Y. M., and de Swart, H. E. (2022). Turbidity maxima in estuarine networks: dependence on fluvial sediment input and local deepening/narrowing with an exploratory model. *Frontiers in Marine Science*.

Zitman, T. J. and Schuttelaars, H. M. (2012). Importance of cross-channel bathymetry and eddy viscosity parameterisation in modelling estuarine flow. *Ocean Dynamics*, 62(4):603–631.

A

A.1 Leading order full solution

The non-dimensional equations of motion for the leading order read

$$\frac{\partial u_0}{\partial t} = -\frac{\partial \eta_0}{\partial x} + \hat{A}_v \frac{\partial^2 u_0}{\partial \tilde{z}^2}, \tag{A.1}$$

$$\frac{\partial u_0}{\partial x} + \frac{\partial w_0}{\partial z} - \frac{L_{tide}}{l_b} u_0 = 0, \tag{A.2}$$

$$\frac{\partial \eta_0}{\partial \tilde{t}} + \frac{\partial}{\partial \tilde{x}} \int_{-H}^{0} u_0 d\tilde{z} - \frac{L_{tide}}{l_b} \int_{-H}^{0} u_0 d\tilde{z} = 0, \tag{A.3}$$

The leading order equations allow the following solutions for u_{02}, w_{02} and η_{02}:

$$(u_{02}, w_{02}, \eta_{02}) = \Re\{(\hat{u}_{02}, \hat{w}_{02}, \hat{\eta}_{02}) e^{-it}\}, \tag{A.4}$$

where $\Re.$ represents the real part of the variables. Substituting these expressions in the momentum equation removes the time dependence and transforms it into an ordinary differential equation (ODE) with only a spatial dependence, as:

$$-i\hat{u}_{02} = -g \frac{\partial \hat{\eta}_{02}}{\partial x} + A_v \frac{\partial^2 \hat{u}_{02}}{\partial z^2}, \tag{A.5}$$

The general solution of equation A.5 is:

$$\hat{u}_{02} = C_1 e^{\gamma z} + C_2 e^{-\gamma z} - \frac{ig}{\omega} \frac{\partial \hat{\eta}_{02}}{\partial x} \tag{A.6}$$

where $\gamma = \sqrt{-i\omega/A_v}$. The solution to this equation can be found by applying boundary conditions in the vertical. The first boundary condition simplifies the equation as:

$$\hat{u}_{02} = C \cosh \gamma z - \frac{ig}{\omega} \frac{\partial \hat{\eta}_{02}}{\partial x} \tag{A.7}$$

Now, applying the second boundary condition in the vertical gives the full expression for the leading order horizontal velocity:

$$\hat{u}_{02}(x, z) = \frac{ig}{\omega} \frac{\partial \hat{\eta}_{02}}{\partial x} \left(\alpha \cosh(\gamma z) - H \right), \tag{A.8}$$

where $\alpha = s_f(A_v\gamma \sinh(\gamma H) + s_f \cosh(\gamma H))^{-1}$. The solution for $\hat{w}_{02}$ is found by substituting A.8 in the continuity equation, integrating over z and by making use of the second boundary condition at $z = 0$:

$$\hat{w}_{02}(x,z) = -\frac{ig}{\omega}\left(\frac{\alpha}{\gamma}\sinh(\gamma z) - z\right)\left(\frac{\partial^2\hat{\eta}_{02}}{\partial x^2} + \frac{1}{l_b}\frac{\partial\hat{\eta}_{02}}{\partial x}\right) - i\hat{\eta}_{02} \tag{A.9}$$

The second boundary condition at $z = -H$ transforms the solution for $\hat{w}_{02}$ in a ODE for $\hat{\eta}_{02}$:

$$\frac{\partial^2\hat{\eta}_{02}}{\partial x^2} + \frac{1}{l_b}\frac{\partial\hat{\eta}_{02}}{\partial x} - \frac{\omega^2}{g\left(\frac{\alpha}{\gamma}\sinh(\gamma H) - H\right)}\hat{\eta}_{02} = 0 \tag{A.10}$$

This equation has the general solution of the form:

$$\hat{\eta}_{02}(x) = A_1 e^{k_1 x} + A_2 e^{k_2 x} \tag{A.11}$$

The wavenumbers k_1 and k_2 are the roots of the ODE in $\hat{\eta}_{02}$ and given by:

$$k_{1,2} = \frac{-\frac{1}{l_b} \pm \sqrt{\left(\frac{1}{l_b}\right)^2 + \frac{4\omega^2}{\frac{\alpha}{\gamma}\sinh(\gamma\tilde{H}) - \tilde{H}}}}{2} \tag{A.12}$$

Now with the use of the boundary condition in the horizontal direction at the seaward side, it follows that $A_1 + A_2 = Z_{M_2}$. From the boundary condition at $x = 0$, it follows that $\frac{\partial\hat{\eta}_{02}}{\partial x} = 0$. This leads to the following algebraic expressions for the constants A_1 and A_2:

$$A_1 = \frac{k_2}{k_2 e^{k_1 L} + k_1 e^{k_2 L}},$$

$$A_2 = -\frac{k_1}{k_2 e^{k_1 L} + k_1 e^{k_2 L}}.$$